

Precise limits on the charge-2=3 U1 vector leptoquark

by

Arvind Bhaskar, Diganta Das, Tanumoy Mandal, Subhadip Mitra, Cyrin Neeraj

in

PHYSICAL REVIEW D

Report No: IIIT/TR/2021/-1



Centre for Computational Natural Sciences and Bioinformatics
International Institute of Information Technology
Hyderabad - 500 032, INDIA
August 2021

Precise limits on the charge-2/3 U_1 vector leptoquark

Arvind Bhaskar^{⊗,1,*} Diganta Das,^{1,2,†} Tanumoy Mandal^{⊗,3,‡} Subhadip Mitra^{⊗,1,§} and Cyrin Neeraj^{1,||}

¹Center for Computational Natural Sciences and Bioinformatics,

International Institute of Information Technology, Hyderabad 500 032, India

²Department of Physics and Astrophysics, University of Delhi, Delhi 110 007, India

³Indian Institute of Science Education and Research, Thiruvananthapuram, Vithura, Kerala 695 551, India



(Received 6 May 2021; accepted 16 July 2021; published 16 August 2021)

The U_1 leptoquark is known to be a suitable candidate for explaining the semileptonic B -decay anomalies. We derive precise limits on its parameter space relevant for the anomalies from the current LHC high- p_T dilepton data. We consider an exhaustive list of possible B -anomalies-motivated simple scenarios with one or two new couplings that can also be used as templates for obtaining bounds on more complicated scenarios. To obtain precise limits, we systematically consider all possible U_1 production processes that can contribute to the dilepton searches, including the resonant pair and single productions, nonresonant t -channel U_1 exchange, as well as its large interference with the Standard Model background. We demonstrate how the inclusion of resonant production contributions in the dilepton signal can lead to appreciably improved exclusion limits. We point out new search channels of U_1 that can act as unique tests of the flavor-motivated models. The template scenarios can also be used for future U_1 searches at the LHC. We compare the LHC limits with other relevant flavor bounds and find that a TeV-scale U_1 can accommodate both $R_{D^{(*)}}$ and $R_{K^{(*)}}$ anomalies while satisfying all the bounds.

DOI: [10.1103/PhysRevD.104.035016](https://doi.org/10.1103/PhysRevD.104.035016)

I. INTRODUCTION

The concept of lepton flavor universality, a key prediction of the Standard Model (SM), seems to be in tension with the present experimental measurements of some semileptonic B -meson decays [1–11]. Differences between theoretical predictions and experimental measurements, hinting toward the existence of some physics beyond the SM (BSM), have been observed in the $R_{D^{(*)}}$ and $R_{K^{(*)}}$ observables:

$$R_{D^{(*)}} = \frac{\mathcal{B}(B \rightarrow D^{(*)} \tau \bar{\nu})}{\mathcal{B}(B \rightarrow D^{(*)} \hat{\ell} \bar{\nu})} \quad \text{and} \quad R_{K^{(*)}} = \frac{\mathcal{B}(B \rightarrow K^{(*)} \mu^+ \mu^-)}{\mathcal{B}(B \rightarrow K^{(*)} e^+ e^-)}. \quad (1)$$

We use $\hat{\ell}$ to denote the light charged leptons, e or μ and $\mathcal{B}(x \rightarrow y)$ for the $x \rightarrow y$ decay branching ratio (BR). The experimental values of R_D and R_{D^*} exceed their SM

predictions by 1.4σ and 3.1σ , respectively [12–15] (combined excess of 3.1σ in $R_{D^{(*)}}$, according to the 2019 world averages [16]), whereas, the R_K and R_{K^*} measurements [17,18] are smaller than the theoretical predictions by about 3.1σ [19,20].

A TeV-scale vector leptoquark (vLQ), a color-triplet vector boson with nonzero lepton and baryon numbers, is considered to be a suitable candidate to address these anomalies in the literature [21–50].¹ It is shown in [37] that a charge-2/3 weak-singlet vLQ, $U_1 \equiv (\mathbf{3}, \mathbf{1}, 2/3)$, can resolve both $R_{D^{(*)}}$ and $R_{K^{(*)}}$ anomalies simultaneously. If the vLQ is really responsible for these anomalies, it is then essential to scrutinize its parameter space that can address the anomalies simultaneously while satisfying all relevant experimental bounds. In the literature, various flavor and collider data have already been used in this context. However, we find that even though a lot of emphasis has been put on obtaining regions of parameter space that are either ruled out or favored by the observed anomalies and other flavor data, relatively less attention has been paid to obtain *precise* bounds from the Large Hadron Collider (LHC) data.

It is known that the regions of parameter spaces favored by the flavor anomalies in various leptoquark (LQ) models are already in tension with the high- p_T dilepton data [29,41,76–81]. In this paper, we specifically investigate

¹See Refs. [51–75] and the references therein for other recent phenomenological studies on LQs.

*arvind.bhaskar@research.iiit.ac.in

†diganta.das@iiit.ac.in

‡tanumoy@iisertvm.ac.in

§subhadip.mitra@iiit.ac.in

||cyrin.neeraj@research.iiit.ac.in

Published by the American Physical Society under the terms of the [Creative Commons Attribution 4.0 International license](https://creativecommons.org/licenses/by/4.0/). Further distribution of this work must maintain attribution to the author(s) and the published article's title, journal citation, and DOI. Funded by SCOAP³.

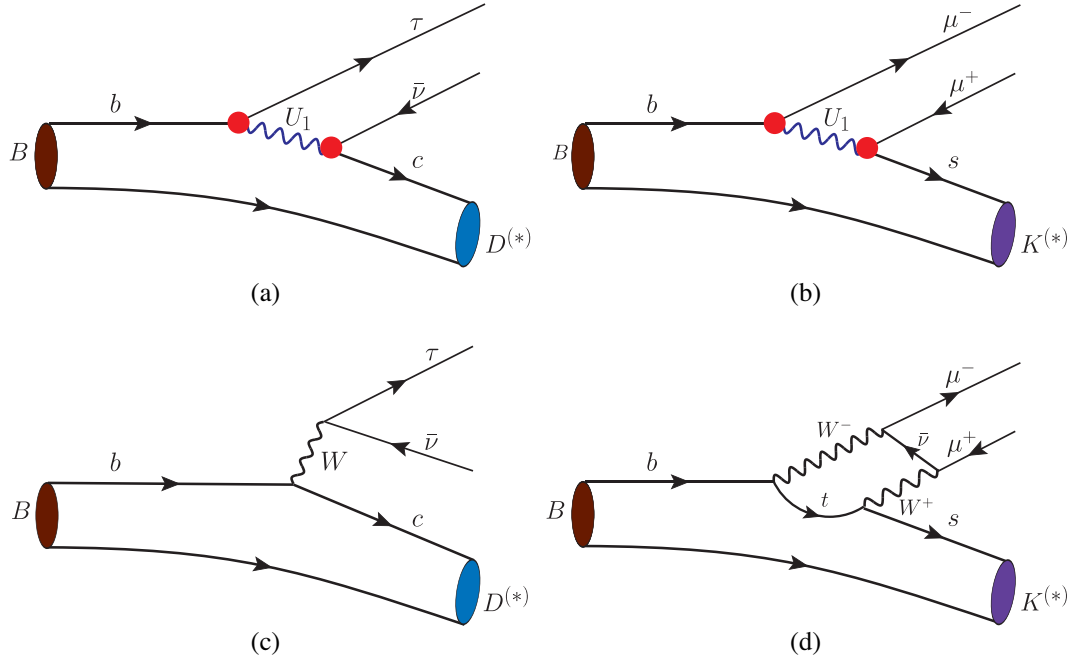


FIG. 1. Representative leading order diagrams showing the $B \rightarrow D^{(*)}\tau\bar{\nu}$ and $B \rightarrow K^{(*)}\mu^+\mu^-$ decays: the tree level U_1 contribution to (a) $B \rightarrow D^{(*)}\tau\bar{\nu}$ and (b) $B \rightarrow K^{(*)}\mu^+\mu^-$, and (c) and (d) the corresponding SM processes, respectively.

the case of U_1 and argue that the bounds from the LHC data might actually be underestimated and, in some regions of the parameter space, the data could be more constraining than what has been considered so far if one systematically computes all relevant processes and considers the latest direct search limits. As we see, different production processes of U_1 contribute to the dilepton or mono-lepton plus missing energy (MET) signals affecting various kinematic distributions. When incorporated in the statistical analysis, they can give strong bounds on the unknown LQ- $q-\ell$ (where ℓ can be any charged lepton) couplings together. However, while most of these processes contribute constructively to the signal, a significant contribution (in fact, the most dominant one, in some cases) comes from the nonresonant t -channel U_1 exchange process that interferes destructively with the SM background. Hence, there is a competition among the U_1 production processes, which are highly sensitive to the U_1 parameters. Usually, the contribution of the resonant production processes (i.e., pair and single productions) to the $\ell\ell$ or $\ell + \cancel{E}_T$ signals are ignored assuming that it would give only minor corrections. However, we find, especially in the lower mass region, that the resonant productions' effect on the exclusion could be significant. In this paper, we systematically put together all the sources of resonant and nonresonant dilepton events in our analysis and obtain robust and precise limits on the U_1 parameters to date.

To contribute to $R_{D^{(*)}}$, a U_1 must couple to the third-generation lepton(s) and, second and third-generation quarks [see Fig. 1(a), assuming that it does not alter the

denominators in Eq. (1)], and to contribute to the $R_{K^{(*)}}$ observables, it should couple to the second-generation leptons [see Fig. 1(b)]. Within the SM, the $b \rightarrow c\tau\bar{\nu}$ decay is mediated by a tree-level charge current interaction, and the neutral current $b \rightarrow s\mu^+\mu^-$ decay occurs through a loop. However, the U_1 LQ can mediate both the flavor-changing transitions, $b \rightarrow c\tau\bar{\nu}$ and $b \rightarrow s\mu^+\mu^-$ at the tree level, as shown in Fig. 1. Here, we adopt a bottom-up approach and construct all possible minimal or next-to-minimal scenarios within the U_1 LQ model with one or two new couplings at a time that can accommodate either the $R_{D^{(*)}}$ or the $R_{K^{(*)}}$ anomalies. These scenarios can be used as templates to obtain bounds on more complicated scenarios (as explained in Ref. [81] for the S_1 LQ).

There is another motivation for considering various minimal scenarios with different coupling combinations. An effective field theory suitable for describing the outcomes of low-energy experiments is not well suited for high-energy collider experiments where some of the heavy degrees of freedom are directly accessible. The SM-like Wilson operator, $\mathcal{O}_{v_L} = [\bar{c}\gamma^\mu P_L b][\bar{\tau}\gamma_\mu P_L \nu]$ plays the most important role in the $R_{D^{(*)}}$ observables. However, by looking only at this operator, it is not obvious that the $\ell\ell$ data would lead to strong bounds, and the interference between the new physics and the SM background processes would play the prominent role in determining the bounds. Scenarios with very different LHC signatures can lead to the same effective operator (we discuss such an example later). Hence, even though these two scenarios would look similar in low-energy experiments, the limits from LHC would be different.

TABLE I. Summary of LQ mass exclusion limits from recent direct searches by the CMS (ATLAS) Collaboration. We recast some of the recent scalar searches (marked with “*”) for better limits on U_1 than the ones for vLQs.

	Integrated	Scalar LQ	Vector LQ, $\kappa = 0$	Vector LQ, $\kappa = 1$
	Luminosity [fb^{-1}]	Mass [GeV]	Mass [Gev]	Mass [GeV]
LQ $\rightarrow t\nu(\mathcal{B} = 1.0)$ [85,87]	35.9 (36.1)	1020(992)	1460	1780
LQ $\rightarrow q\nu(\mathcal{B} = 1.0)$ [85]	35.9	980	1410	1790
LQ $\rightarrow b\nu(\mathcal{B} = 1.0)$ [85,87]	35.9 (36.1)	1100(968)	1475	1810
LQ $\rightarrow b\tau/t\nu(\mathcal{B} = 0.5)$ [88]	137	950	1290	1650
LQ $\rightarrow b\tau(\mathcal{B} = 1.0)$ [87] *	(36.1)	(1000)
LQ $\rightarrow \mu j(\mathcal{B} = 1.0)$ [86] *	(139)	(1733)
LQ $\rightarrow \mu c(\mathcal{B} = 1.0)$ [86]	(139)	(1680)
LQ $\rightarrow \mu b(\mathcal{B} = 1.0)$ [86] *	(139)	(1721)

In the case of the scalar LQ S_1 , we have seen the dilepton data putting stronger bounds than the monolepton plus MET data [81]. Hence, in this paper, we consider only the dilepton ($\tau\tau$ and $\mu\mu$ [82,83]) data to put bounds on the regions of U_1 parameter space relevant for the $R_{D^{(*)}}$ and $R_{K^{(*)}}$ observables. Unlike the existing bounds on LQ masses from their pair production searches at the LHC, the bounds thus obtained are model dependent (i.e., they depend on unknown couplings). However, for large new couplings they become more restrictive than the pair production ones. We obtain the LHC bounds for various scenarios with different coupling structures and show that they are competitive and complimentary to other flavor bounds. Also, these bounds are independent of other known theoretical constraints on the U_1 parameter space. Obtaining them requires a systematic consideration of different LQ signal processes at the LHC (including their interference with the SM backgrounds which plays the dominant role in determining the bounds). Here, for systematics, we largely follow the analysis of Ref. [81] (where a similar analysis was done for a S_1 -type scalar LQ that can alleviate the $R_{D^{(*)}}$ anomalies).

Before we proceed further, we review the direct detection bounds on LQs that couple with second- and third-generation fermions. Assuming the extra gluon- U_1 coupling $\kappa = 0$ (we follow the same convention as [84]), a recent LQ pair production search at the CMS detector has excluded vLQs with masses below 1460 GeV for $\mathcal{B}(\text{LQ} \rightarrow t\nu) = 1$ [85]. For a vLQ decaying to a light quark and a neutrino with 100% BR, the mass exclusion limit is at 1410 GeV. In the case where it decays to a bottom quark and a neutrino, the limit goes to 1475 GeV. If the vLQ decays to a top quark + a neutrino and a bottom quark + τ with equal BRs, then the mass points below 1115 GeV are excluded. For $\kappa = 1$, the limits go up [85]. Pair produced scalar LQs decaying to a light quark and a neutrino with branching ratio unity can be excluded up to 980 GeV. A scalar LQ decaying to a b -quark and a neutrino with a 100% branching ratio can be excluded up to 1100 GeV [85]. The ATLAS experiment searched for scalar LQs

decaying to the following final states, μc , $\mu +$ a light quark, and μb [86]. The exclusion limits from these channels and the above are summarized in Table I.

The paper is organized as follows. In the next section, we introduce the U_1 LQ model and the relevant scenarios. In Section III, we describe its LHC phenomenology. In Section IV, we discuss the dilepton search and their recasts. In Section V, we present the numerical results, and finally, in Section VI, we conclude.

II. THE U_1 LEPTOQUARK MODEL

The interaction between U_1 and the SM quarks and leptons can be expressed as [89–92]

$$\mathcal{L} \supset x_{1ij}^{LL} \bar{Q}^i \gamma_\mu U_1^\mu P_L L^j + x_{1ij}^{RR} \bar{d}_R^i \gamma_\mu U_1^\mu P_R \ell_R^j + \text{H.c.}, \quad (2)$$

if we ignore the diquark interactions which are severely constrained by the proton decay bounds. Here, Q_i and L_j denote the SM left-handed quark and lepton doublets, respectively, and d_R^i and ℓ_R^j are the down-type right-handed quarks and leptons, respectively. The indices $i, j = \{1, 2, 3\}$ stand for quark and lepton generations; i.e., x_{1ij}^{LL} and x_{1ij}^{RR} are 3×3 matrices in flavor space. In general, these matrices are complex. We, however, simply assume them to be real since the LHC would be mostly insensitive to their complex natures. Global fits to experimental data with complex couplings are similar to the fits obtained with real couplings, albeit with slightly greater significance [93,94]. Hence, predictions for flavor observables with complex couplings are expected to be similar to the ones obtained with purely real couplings. Moreover, since we are interested in only those U_1 scenarios that can accommodate the $R_{D^{(*)}}$ and $R_{K^{(*)}}$ anomalies, we further simplify the x_{1ij}^{LL} and x_{1ij}^{RR} matrices by setting all the components that do not participate directly in these decays to zero. We refer to any type of neutrinos simply as ν , i.e., without any flavor index as this would not affect our LHC analysis. As the $b \rightarrow c\tau\bar{\nu}$ and $b \rightarrow s\mu^+\mu^-$ decays involve independent couplings, we

analyze the $R_{D^{(*)}}$ - and $R_{K^{(*)}}$ -anomalies-motivated scenarios separately.²

A. $R_{D^{(*)}}$ scenarios

In the SM, the $b \rightarrow c\tau\bar{\nu}$ transition is a tree-level charged-current-mediated process and the Lagrangian responsible for it can be written as

$$\mathcal{L}_{\text{SM}} = -\frac{4G_F}{\sqrt{2}}V_{cb}\mathcal{O}_{V_L} = -\frac{4G_F}{\sqrt{2}}V_{cb}[\bar{c}\gamma^\mu P_L b][\bar{\tau}\gamma_\mu P_L \nu_\tau]. \quad (3)$$

New physics can generate additional contributions to the $b \rightarrow c\tau\bar{\nu}$ transition in the form of four-fermion operators. The most general form of the Lagrangian can be written as [95]

$$\mathcal{L} \supset -\frac{4G_F}{\sqrt{2}}V_{cb}[(1 + \mathcal{C}_{V_L})\mathcal{O}_{V_L} + \mathcal{C}_{V_R}\mathcal{O}_{V_R} + \mathcal{C}_{S_L}\mathcal{O}_{S_L} + \mathcal{C}_{S_R}\mathcal{O}_{S_R} + \mathcal{C}_{T_R}\mathcal{O}_{T_R}], \quad (4)$$

where the Wilson coefficient corresponding to an operator \mathcal{O}_i is denoted as \mathcal{C}_i . The operators have three different Lorentz structures:

(i) Vector:

$$\begin{cases} \mathcal{O}_{V_L} = [\bar{c}\gamma^\mu P_L b][\bar{\tau}\gamma_\mu P_L \nu] \\ \mathcal{O}_{V_R} = [\bar{c}\gamma^\mu P_R b][\bar{\tau}\gamma_\mu P_L \nu] \end{cases}$$

(ii) Scalar:

$$\begin{cases} \mathcal{O}_{S_L} = [\bar{c}P_L b][\bar{\tau}P_L \nu] \\ \mathcal{O}_{S_R} = [\bar{c}P_R b][\bar{\tau}P_L \nu] \end{cases}$$

(iii) Tensor: $\mathcal{O}_{T_L} = [\bar{c}\sigma^{\mu\nu}P_L b][\bar{\tau}\sigma_{\mu\nu}P_L \nu]$.

From Fig. 1 we see that the $\bar{c}\nu U_1$ and $\bar{b}\tau U_1$ couplings have to be nonzero for U_1 to contribute in the $b \rightarrow c\tau\bar{\nu}$ process. We make the following flavor *Ansatz* for simplicity:

$$x_1^{LL} = \begin{pmatrix} 0 & 0 & 0 \\ 0 & 0 & \lambda_{23}^L \\ 0 & 0 & \lambda_{33}^L \end{pmatrix}, \quad x_1^{RR} = \begin{pmatrix} 0 & 0 & 0 \\ 0 & 0 & 0 \\ 0 & 0 & \lambda_{33}^R \end{pmatrix}. \quad (5)$$

Given the *Ansätze* of the five operators listed above, only \mathcal{O}_{V_L} and \mathcal{O}_{S_L} can be generated by U_1 , i.e., $\mathcal{C}_{V_R}^{U_1} = \mathcal{C}_{S_R}^{U_1} = \mathcal{C}_{T_R}^{U_1} = 0$. Note that the simplified assumption of several zeros in the coupling matrices are purely phenomenological. This may not be strictly valid in some specific models, e.g., in the models in Refs. [66,71] where the LQ induced flavor structures are parametrized by Froggatt-Nielsen charges.

The nonzero coefficients, \mathcal{C}_{V_L} and \mathcal{C}_{S_L} , can be written in terms of the $\bar{c}\nu U_1$ and $\bar{b}\tau U_1$ couplings,

$$\left. \begin{cases} \mathcal{C}_{V_L}^{U_1} = \frac{1}{2\sqrt{2}G_F V_{cb}} \frac{\lambda_{c\nu}^L (\lambda_{b\tau}^L)^*}{M_{U_1}^2} \\ \mathcal{C}_{S_L}^{U_1} = -\frac{1}{2\sqrt{2}G_F V_{cb}} \frac{2\lambda_{c\nu}^L (\lambda_{b\tau}^R)^*}{M_{U_1}^2} \end{cases} \right\}. \quad (6)$$

The actual relationship of $\lambda_{c\nu}^L$ and $\lambda_{b\tau}^{L/R}$ with λ_{23}^L and $\lambda_{33}^{L/R}$, defined in Eq. (5), varies from scenario to scenario. We can express the ratios, $r_{D^{(*)}} = R_{D^{(*)}}/R_{D^{(*)}}^{\text{SM}}$ in terms of the nonzero Wilson coefficients as [96]

$$r_D \equiv \frac{R_D}{R_D^{\text{SM}}} \approx |1 + \mathcal{C}_{V_L}^{U_1}|^2 + 1.02|\mathcal{C}_{S_L}^{U_1}|^2 + 1.49\text{Re}[(1 + \mathcal{C}_{V_L}^{U_1})\mathcal{C}_{S_L}^{U_1*}], \quad (7)$$

$$r_{D^*} \equiv \frac{R_{D^*}}{R_{D^*}^{\text{SM}}} \approx |1 + \mathcal{C}_{V_L}^{U_1}|^2 + 0.04|\mathcal{C}_{S_L}^{U_1}|^2 - 0.11\text{Re}[(1 + \mathcal{C}_{V_L}^{U_1})\mathcal{C}_{S_L}^{U_1*}]. \quad (8)$$

There are two other observables where nonzero $\mathcal{C}_{V_L}^{U_1}$ and $\mathcal{C}_{S_L}^{U_1}$ would contribute to—the longitudinal D^* polarization $F_L(D^*)$ and the longitudinal τ polarization asymmetry $P_\tau(D^*)$. They have been measured by the Belle Collaboration [10,11,97]. For our purpose, we can express $F_L(D^*)$ and $P_\tau(D^*)$ as [96]

$$f_L(D^*) \equiv \frac{F_L(D^*)}{F_L^{\text{SM}}(D^*)} \approx \frac{1}{r_{D^*}} \{ |1 + \mathcal{C}_{V_L}^{U_1}|^2 + 0.08|\mathcal{C}_{S_L}^{U_1}|^2 - 0.24\text{Re}[(1 + \mathcal{C}_{V_L}^{U_1})\mathcal{C}_{S_L}^{U_1*}] \}, \quad (9)$$

$$p_\tau(D^*) \equiv \frac{P_\tau(D^*)}{P_\tau^{\text{SM}}(D^*)} \approx \frac{1}{r_{D^*}} \{ |1 + \mathcal{C}_{V_L}^{U_1}|^2 - 0.07|\mathcal{C}_{S_L}^{U_1}|^2 + 0.22\text{Re}[(1 + \mathcal{C}_{V_L}^{U_1})\mathcal{C}_{S_L}^{U_1*}] \}. \quad (10)$$

²From here onward, we refer to the $R_{D^{(*)}}$ - and $R_{K^{(*)}}$ -anomalies-motivated scenarios simply as $R_{D^{(*)}}$ and $R_{K^{(*)}}$ scenarios for brevity.

A nonzero $\mathcal{C}_{V_L}^{U_1}$ and $\mathcal{C}_{S_L}^{U_1}$ would also contribute to leptonic decays $B_c \rightarrow \tau\nu$ and $B \rightarrow \tau\nu$ as

$$\mathcal{B}(B_c \rightarrow \tau\nu) = \frac{\tau_{B_c} m_{B_c} f_{B_c}^2 G_F^2 |V_{cb}|^2}{8\pi} m_\tau^2 \left(1 - \frac{m_\tau^2}{m_{B_c}^2}\right)^2 \left|1 + \mathcal{C}_{V_L}^{U_1} + \frac{m_{B_c}^2}{m_\tau(m_b + m_c)} \mathcal{C}_{S_L}^{U_1}\right|^2, \quad (11)$$

$$\mathcal{B}(B \rightarrow \tau\nu) = \mathcal{B}(B \rightarrow \tau\nu)_{\text{SM}} \left|1 + \mathcal{C}_{V_L}^{U_1} + \frac{m_B^2}{m_\tau(m_b + m_u)} \mathcal{C}_{S_L}^{U_1}\right|^2 \quad (12)$$

where τ_{B_c} is the lifetime of the B_c meson, f_{B_c} is its decay constant, and $\mathcal{B}(B \rightarrow \tau\nu)_{\text{SM}}$ is the branching ratio within the SM. The LEP data put a constraint on the $B_c \rightarrow \tau\nu$ branching ratio [98] as, $\mathcal{B}(B_c \rightarrow \tau\nu) < 10\%$. The experimental upper bound on the $B \rightarrow \tau\nu$ decay is given as [99] $\mathcal{B}(B \rightarrow \tau\nu) < (1.09 \pm 0.24) \times 10^{-4}$, and the corresponding SM branching ratio is estimated to be [100] $\mathcal{B}(B \rightarrow \tau\nu)_{\text{SM}} = (0.812 \pm 0.054) \times 10^{-4}$. The current bounds on these observables are summarized in Table II. Wherever applicable, we also consider constraints from $B_s - \bar{B}_s$ mixing [see Fig. 2(a)] through the effective Hamiltonian

$$H_{\text{eff}} = (\mathcal{C}_{\text{box}}^{\text{SM}} + \mathcal{C}_{\text{box}}^{U_1})(\bar{s}_L \gamma^\alpha b_L)(\bar{s}_L \gamma_\alpha b_L) \quad (13)$$

where the SM contribution, $\mathcal{C}_{\text{box}}^{\text{SM}}$, and the U_1 contribution, $\mathcal{C}_{\text{box}}^{U_1}$, which generically depends on new coupling(s) as $\sim \lambda^4$, are given as

$$\mathcal{C}_{\text{box}}^{\text{SM}} = \frac{G_F^2}{4\pi^2} (V_{ib} V_{ts})^2 M_W^2 S_0(x_t), \quad (14)$$

$$\mathcal{C}_{\text{box}}^{U_1} = \frac{\lambda^4}{8\pi^2 M_{U_1}^2}. \quad (15)$$

In Eq. (14), the generation indices and possible Cabibbo-Kobayashi-Maskawa (CKM) elements have been omitted as they depend on the scenario that we are interested in. The loop function is the Inami-Lim function [101], $S_0(x_t \equiv m_t^2/m_W^2) \sim 2.37$ [102]. The UT *fit* Collaboration gives the following bounds on the ratio $\mathcal{C}_{\text{box}}^{U_1}/\mathcal{C}_{\text{box}}^{\text{SM}}$ [100]:

$$0.94 < \left|1 + \frac{\mathcal{C}_{\text{box}}^{U_1}}{\mathcal{C}_{\text{box}}^{\text{SM}}}\right| < 1.29. \quad (16)$$

Additionally, whenever $\lambda_{b\tau}^L$ and $\lambda_{s\tau}^L$ are simultaneously nonzero, they contribute to another lepton-flavor-universal operator in a log-enhanced manner through an off-shell photon penguin diagram as [see Fig. 2(b)]

$$\mathcal{L} \supset -\frac{4G_F}{\sqrt{2}} (V_{ib} V_{ts}^*) \mathcal{C}_9^{\text{univ}} \mathcal{O}_9^{\text{univ}} \quad (17)$$

where

$$\mathcal{O}_9^{\text{univ}} = \frac{\alpha}{4\pi} (\bar{s}_L \gamma_\alpha b_L)(\bar{\ell} \gamma^\alpha \ell) \quad \text{and} \quad \mathcal{C}_9^{\text{univ}} = -\frac{1}{V_{ib} V_{ts}^*} \frac{\lambda_{s\tau}^L (\lambda_{b\tau}^L)^*}{3\sqrt{2} G_F M_{U_1}^2} \log(m_b^2/M_{U_1}^2). \quad (18)$$

We consider the 2σ limits from the global fits to the $b \rightarrow s\mu^+\mu^-$ data [103–105] as $-1.27 \leq \mathcal{C}_9^{\text{univ}} \leq -0.51$.

TABLE II. Bounds on the $R_{D^{(*)}}$ -anomalies-motivated scenarios.

Observable	Experimentally allowed range	SM expectation	Ratio	Value
R_D	$0.340 \pm 0.027 \pm 0.013$ [16]	0.299 ± 0.003 [12]	r_D	1.137 ± 0.101
R_{D^*}	$0.295 \pm 0.011 \pm 0.008$ [16]	0.258 ± 0.005 [16]	r_{D^*}	1.144 ± 0.057
$F_L(D^*)$	$0.60 \pm 0.08 \pm 0.035$ [10,11]	0.46 ± 0.04 [106]	$f_L(D^*)$	1.313 ± 0.198
$P_\tau(D^*)$	$-0.38 \pm 0.51_{-0.16}^{+0.21}$ [97]	-0.497 ± 0.013 [95]	$p_\tau(D^*)$	0.766 ± 1.093
$\mathcal{B}(B \rightarrow \tau\nu)$	$< (1.09 \pm 0.24) \times 10^{-4}$ [99]	$(0.812 \pm 0.054) \times 10^{-4}$ [100]		
$\mathcal{B}(B_c \rightarrow \tau\nu)$	$< 10\%$ [98]			

We now consider different scenarios with different combinations of the three couplings λ_{23}^L , λ_{33}^L and λ_{33}^R . As indicated in the Introduction, these scenarios may not always appear very different from each other if we look at them only from the perspective of effective operators, but their LHC phenomenology are different. As a result, the bounds from the LHC data differ within the scenarios. We elaborate this point further shortly.

B. Scenario RD1A

In this scenario, only λ_{23}^L is assumed to be nonzero. This directly generates the following two couplings: $\bar{c}\nu U_1$ and $\bar{s}\tau U_1$. We assume that the U_1 interaction is aligned with the physical basis of the up-type quarks. The interactions with the physical down-type quarks are then obtained by rotating them with the CKM matrix (i.e., by considering mixing among the down-type quarks) [81]. This way, an effective $\bar{b}\tau U_1$ coupling of strength $V_{cb}^* \lambda_{23}^L$ is generated. The interaction Lagrangian now reads as

$$\begin{aligned} \mathcal{L} &\supset \lambda_{23}^L [\bar{c}_L \gamma_\mu \nu_L + \bar{s}_L \gamma_\mu \tau_L] U_1^\mu, \\ &= \lambda_{23}^L [\bar{c}_L \gamma_\mu \nu_L + (V_{cd}^* \bar{d}_L + V_{cs}^* \bar{s}_L + V_{cb}^* \bar{b}_L) \gamma_\mu \tau_L] U_1^\mu \end{aligned} \quad (19)$$

giving

$$\mathcal{C}_{V_L}^{RD1A} = \frac{1}{2\sqrt{2}G_F} \frac{(\lambda_{23}^L)^2}{M_{U_1}^2}, \quad \mathcal{C}_{S_L}^{RD1A} = 0. \quad (20)$$

This implies the observables, $R_{D^{(*)}}$, $F_L(D^*)$, $P_\tau(D^*)$, and $\mathcal{B}(B_{(c)} \rightarrow \tau\nu)$ would receive contributions from U_1 . Due to the off-shell photon-penguin diagram shown in Fig. 2, there will be a log-enhanced lepton-universal contribution to the $b \rightarrow s\ell^+\ell^-$ transition [36]:

$$\mathcal{C}_9^{\text{univ}} = -\frac{V_{cb}V_{cs}^*}{V_{tb}V_{ts}^*} \frac{(\lambda_{23}^L)^2}{3\sqrt{2}G_F M_{U_1}^2} \log(m_b^2/M_{U_1}^2). \quad (21)$$

This scenario would lead to a nonzero contribution to the $B_s - \bar{B}_s$ mixing coefficient as

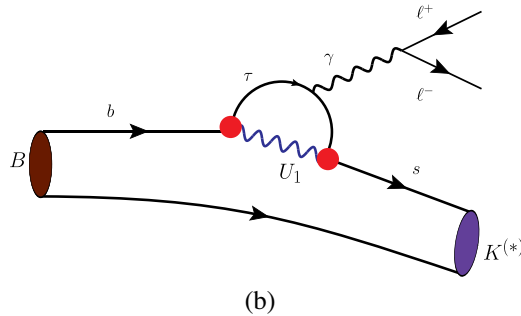
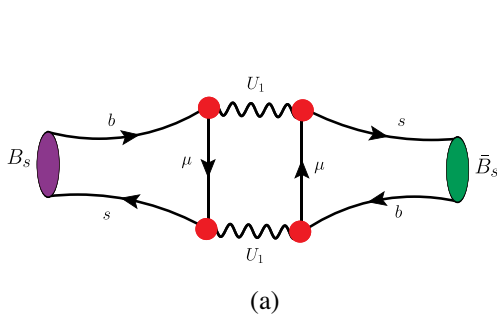


FIG. 2. (a) A representative diagram showing the U_1 contribution to $B_s - \bar{B}_s$ mixing and (b) a U_1 -mediated photon penguin diagram contributing to $b \rightarrow s\ell^+\ell^-$.

$$\mathcal{C}_{\text{box}}^{U_1} = \frac{|V_{cb}|^2 |V_{cs}|^2 (\lambda_{23}^L)^4}{8\pi^2 M_{U_1}^2}. \quad (22)$$

The dominant decay modes of U_1 in this scenario are $U_1 \rightarrow c\bar{\nu}$ and $U_1 \rightarrow s\tau^+$, and both of them share almost 50% BR.

C. Scenario RD1B

In this scenario, only λ_{33}^L is assumed to be nonzero, thus generating the $\bar{b}\tau U_1$ and $\bar{t}\nu U_1$ couplings. Assuming the U_1 interaction to be aligned with the physical basis of the down-type quarks, we generate $\bar{c}\nu U_1$ coupling $V_{cb}\lambda_{33}^L$ through the mixing in the up-type quarks. The interaction Lagrangian is given by

$$\begin{aligned} \mathcal{L} &\supset \lambda_{33}^L [\bar{t}_L \gamma_\mu \nu_L + \bar{b}_L \gamma_\mu \tau_L] U_1^\mu \\ &= \lambda_{33}^L [(V_{ub}\bar{u}_L + V_{cb}\bar{c}_L + V_{tb}\bar{t}_L) \gamma_\mu \nu_L + \bar{b}_L \gamma_\mu \tau_L] U_1^\mu, \end{aligned} \quad (23)$$

and the contributions to the Wilson coefficients are given by

$$\mathcal{C}_{V_L}^{RD1B} = \frac{1}{2\sqrt{2}G_F} \frac{(\lambda_{33}^L)^2}{M_{U_1}^2}, \quad \mathcal{C}_{S_L}^{RD1B} = 0. \quad (24)$$

Like in Scenario RD1A, the observables $R_{D^{(*)}}$, $F_L(D^*)$, $P_\tau(D^*)$, and $\mathcal{B}(B_{(c)} \rightarrow \tau\nu)$ would receive contribution from U_1 in this case too. Here, the dominant decay modes of U_1 are $U_1 \rightarrow t\bar{\nu}$ and $U_1 \rightarrow b\tau^+$ with 50% BR each.

D. Scenario RD2A

In this scenario, we assume λ_{23}^L and λ_{33}^L to be nonzero, and the interaction of U_1 is aligned with the physical basis of the down-type quarks. The interaction Lagrangian can be written as

$$\begin{aligned} \mathcal{L} &\supset [\lambda_{23}^L (\bar{c}_L \gamma_\mu \nu_L + \bar{s}_L \gamma_\mu \tau_L) + \lambda_{33}^L (\bar{t}_L \gamma_\mu \nu_L + \bar{b}_L \gamma_\mu \tau_L)] U_1^\mu \\ &= [\lambda_{23}^L (V_{us}\bar{u}_L \gamma_\mu \nu_L + V_{cs}\bar{c}_L \gamma_\mu \nu_L + V_{ts}\bar{t}_L \gamma_\mu \nu_L + \bar{s}_L \gamma_\mu \tau_L) \\ &\quad + \lambda_{33}^L (V_{ub}\bar{u}_L \gamma_\mu \nu_L + V_{cb}\bar{c}_L \gamma_\mu \nu_L + V_{tb}\bar{t}_L \gamma_\mu \nu_L \\ &\quad + \bar{b}_L \gamma_\mu \tau_L)] U_1^\mu, \end{aligned} \quad (25)$$

where, in the second step, we have assumed mixing among the up-type quarks. In the absence of λ_{23}^R , in this case, $\mathcal{C}_{V_L}^{RD2A}$ is the only nonzero Wilson coefficient, i.e.,

$$\mathcal{C}_{V_L}^{RD2A} = \frac{1}{2\sqrt{2}G_F V_{cb}} \frac{(V_{cs}\lambda_{23}^L + V_{cb}\lambda_{33}^L)\lambda_{33}^L}{M_{U_1}^2}, \quad \mathcal{C}_{S_L}^{RD2A} = 0. \quad (26)$$

In addition to the contribution to the $R_{D^{(*)}}$, $F_L(D^*)$, $P_\tau(D^*)$, and $\mathcal{B}(B_{(c)} \rightarrow \tau\nu)$ processes, we consider the lepton flavor-universal contribution

$$\mathcal{C}_9^{\text{univ}} = -\frac{1}{V_{ib}V_{is}^*} \frac{\lambda_{23}^L\lambda_{33}^L}{3\sqrt{2}G_F M_{U_1}^2} \log(m_b^2/M_{U_1}^2). \quad (27)$$

In this scenario, the $B_s - \bar{B}_s$ mixing coefficient would receive a contribution from U_1

$$\mathcal{C}_{\text{box}}^{U_1} = \frac{(\lambda_{23}^L)^2(\lambda_{33}^L)^2}{8\pi^2 M_{U_1}^2}. \quad (28)$$

Here, U_1 can decay to $c\bar{\nu}$, $s\tau^+$, $t\bar{\nu}$ and $b\tau^+$ final states with comparable BRs.

E. Scenario RD2B

Here, both λ_{23}^L and λ_{33}^R are nonzero. Ignoring possible CKM-suppressed couplings, the interaction Lagrangian is given by

$$\begin{aligned} \mathcal{L} \supset & [\lambda_{23}^L(\bar{c}_L\gamma_\mu\nu_L + \bar{s}_L\gamma_\mu\tau_L) + \lambda_{33}^L(\bar{t}_L\gamma_\mu\nu_L + \bar{b}_L\gamma_\mu\tau_L) + \lambda_{33}^R\bar{b}_R\gamma_\mu\tau_R]U_1^\mu \\ & = [\lambda_{23}^L(V_{us}\bar{u}_L\gamma_\mu\nu_L + V_{cs}\bar{c}_L\gamma_\mu\nu_L + V_{ts}\bar{t}_L\gamma_\mu\nu_L + \bar{s}_L\gamma_\mu\tau_L) \\ & \quad + \lambda_{33}^L(V_{ub}\bar{u}_L\gamma_\mu\nu_L + V_{cb}\bar{c}_L\gamma_\mu\nu_L + V_{tb}\bar{t}_L\gamma_\mu\nu_L + \bar{b}_L\gamma_\mu\tau_L) + \lambda_{33}^R\bar{b}_R\gamma_\mu\tau_R]U_1^\mu. \end{aligned} \quad (31)$$

This Lagrangian contributes to \mathcal{C}_{V_L} and \mathcal{C}_{S_L} as

$$\mathcal{C}_{V_L}^{RD3} = \frac{1}{2\sqrt{2}G_F V_{cb}} \frac{(V_{cb}\lambda_{33}^L + V_{cs}\lambda_{23}^L)\lambda_{33}^L}{M_{U_1}^2}, \quad \mathcal{C}_{S_L}^{RD3} = -\frac{1}{\sqrt{2}G_F V_{cb}} \frac{(V_{cb}\lambda_{33}^L + V_{cs}\lambda_{23}^L)\lambda_{33}^R}{M_{U_1}^2}. \quad (32)$$

The lepton flavor-universal contribution through the off-shell photon penguin diagram is

$$\mathcal{C}_9^{\text{univ}} = -\frac{1}{V_{ib}V_{is}^*} \frac{\lambda_{23}^L\lambda_{33}^L}{3\sqrt{2}G_F M_{U_1}^2} \log(m_b^2/M_{U_1}^2). \quad (33)$$

The contribution of U_1 to the $B_s - \bar{B}_s$ mixing coefficient is given as

$$\mathcal{C}_{\text{box}}^{U_1} = \frac{(\lambda_{23}^L)^2(\lambda_{33}^L)^2}{8\pi^2 M_{U_1}^2}. \quad (34)$$

$$\begin{aligned} \mathcal{L} \supset & [\lambda_{23}^L(\bar{c}_L\gamma_\mu\nu_L + \bar{s}_L\gamma_\mu\tau_L) + \lambda_{33}^R\bar{b}_R\gamma_\mu\tau_R]U_1^\mu \\ & = [\lambda_{23}^L(V_{us}\bar{u}_L\gamma_\mu\nu_L + V_{cs}\bar{c}_L\gamma_\mu\nu_L + V_{ts}\bar{t}_L\gamma_\mu\nu_L \\ & \quad + \bar{s}_L\gamma_\mu\tau_L) + \lambda_{33}^R\bar{b}_R\gamma_\mu\tau_R]U_1^\mu, \end{aligned} \quad (29)$$

where, once again in the second step we have assumed mixing among the up-type quarks. This gives the following contribution to \mathcal{C}_{S_L} :

$$\mathcal{C}_{V_L}^{RD2B} = 0, \quad \mathcal{C}_{S_L}^{RD2B} = -\frac{V_{cs}}{\sqrt{2}G_F V_{cb}} \frac{\lambda_{23}^L\lambda_{33}^R}{M_{U_1}^2}. \quad (30)$$

Here, $R_{D^{(*)}}$, $F_L(D^*)$, $P_\tau(D^*)$, and $\mathcal{B}(B_{(c)} \rightarrow \tau\nu)$ would receive contributions from U_1 . The dominant decay modes of U_1 are $U_1 \rightarrow c\bar{\nu}$, $U_1 \rightarrow s\tau^+$, and $U_1 \rightarrow b\tau^+$. Note that even though $\lambda_{33}^L = 0$ in this scenario, a small \mathcal{C}_{V_L} can be generated from effective λ_{33}^L coupling if, instead of up-type quark mixing, one assumes mixing in the down sector (like in Scenario RD1A).

F. Scenario RD3

All the three free couplings λ_{23}^L , λ_{33}^L , and λ_{33}^R are free to vary. Assuming mixing in the up-type quark sector, the interaction Lagrangian is given by

In this scenario, U_1 dominantly decays to $c\bar{\nu}$, $s\tau^+$, $t\bar{\nu}$, and $b\tau^+$ final states.

G. $R_{K^{(*)}}$ scenarios

A general Lagrangian for $b \rightarrow s\mu^+\mu^-$ transition can be written as [107,108]

$$\mathcal{L} \supset \frac{4G_F}{\sqrt{2}} V_{ib}V_{is}^* \sum_{i=9,10,S,P} (\mathcal{C}_i\mathcal{O}_i + \mathcal{C}'_i\mathcal{O}'_i), \quad (35)$$

where the Wilson coefficients are evaluated at $\mu_{\text{ren}} = m_b$. The operators are given by

$$\begin{aligned}\mathcal{O}_9 &= \frac{\alpha}{4\pi}(\bar{s}_L\gamma_\alpha b_L)(\bar{\mu}\gamma^\alpha\mu), & \mathcal{O}'_9 &= \frac{\alpha}{4\pi}(\bar{s}_R\gamma_\alpha b_R)(\bar{\mu}\gamma^\alpha\mu), \\ \mathcal{O}_{10} &= \frac{\alpha}{4\pi}(\bar{s}_L\gamma_\alpha b_L)(\bar{\mu}\gamma^\alpha\gamma_5\mu), & \mathcal{O}'_{10} &= \frac{\alpha}{4\pi}(\bar{s}_R\gamma_\alpha b_R)(\bar{\mu}\gamma^\alpha\gamma_5\mu), \\ \mathcal{O}_S &= \frac{\alpha}{4\pi}(\bar{s}_L b_R)(\bar{\mu}\mu), & \mathcal{O}'_S &= \frac{\alpha}{4\pi}(\bar{s}_R b_L)(\bar{\mu}\mu), \\ \mathcal{O}_P &= \frac{\alpha}{4\pi}(\bar{s}_L b_R)(\bar{\mu}\gamma_5\mu), & \mathcal{O}'_P &= \frac{\alpha}{4\pi}(\bar{s}_R b_L)(\bar{\mu}\gamma_5\mu),\end{aligned}$$

where α is the fine-structure constant. Keeping the $R_{K^{(*)}}$ observables in mind, we make the following simple *Ansatz*:

$$x_1^{LL} = \begin{pmatrix} 0 & 0 & 0 \\ 0 & \lambda_{22}^L & 0 \\ 0 & \lambda_{32}^L & 0 \end{pmatrix}; \quad x_1^{RR} = \begin{pmatrix} 0 & 0 & 0 \\ 0 & \lambda_{22}^R & 0 \\ 0 & \lambda_{32}^R & 0 \end{pmatrix}. \quad (36)$$

The U_1 contribution to the Wilson coefficients can be written in terms of the $\bar{b}\mu U_1$ and $\bar{s}\mu U_1$ couplings in general as

$$\left. \begin{aligned}\mathcal{C}_9^{U_1} &= -\mathcal{C}_{10}^{U_1} = \frac{\pi}{\sqrt{2}G_F V_{ib} V_{is}^* \alpha} \frac{\lambda_{s\mu}^L (\lambda_{b\mu}^L)^*}{M_{U_1}^2} \\ \mathcal{C}_S^{U_1} &= -\mathcal{C}_P^{U_1} = \frac{\sqrt{2}\pi}{G_F V_{ib} V_{is}^* \alpha} \frac{\lambda_{s\mu}^L (\lambda_{b\mu}^R)^*}{M_{U_1}^2} \\ \mathcal{C}'_9^{U_1} &= \mathcal{C}'_{10}^{U_1} = \frac{\pi}{\sqrt{2}G_F V_{ib} V_{is}^* \alpha} \frac{\lambda_{s\mu}^R (\lambda_{b\mu}^{R*})}{M_{U_1}^2} \\ \mathcal{C}'_S^{U_1} &= \mathcal{C}'_P^{U_1} = \frac{\sqrt{2}\pi}{G_F V_{ib} V_{is}^* \alpha} \frac{\lambda_{s\mu}^R (\lambda_{b\mu}^{L*})}{M_{U_1}^2}\end{aligned}\right\}. \quad (37)$$

Like in the $R_{D^{(*)}}$ scenarios, the relationship between $\{\lambda_{s\mu}^{L/R}, \lambda_{b\mu}^{L/R}\}$ with $\{\lambda_{22}^{L/R}, \lambda_{32}^{L/R}\}$ would depend on the particulars of the scenario we consider. The relevant global fits of the Wilson coefficients to the $b \rightarrow s\mu^+\mu^-$ data are taken from Refs. [104,105,109] and are listed in Table III.

H. Scenario RK1A

In this scenario, only λ_{22}^L is nonzero. This generates the $\bar{s}\mu U_1$ coupling. The $\bar{b}\mu U_1$ coupling is generated via CKM mixing in the down-quark sector (as in Scenario RD1A and Scenario RD1B). The interaction Lagrangian can be written as

$$\mathcal{L} \supset \lambda_{22}^L [\bar{c}_L \gamma_\mu \nu_L + (V_{cd}^* \bar{d}_L + V_{cs}^* \bar{s}_L + V_{cb}^* \bar{b}_L) \gamma_\mu \mu_L] U_1^\mu. \quad (38)$$

This Lagrangian contributes to the following coefficients:

$$\mathcal{C}_9^{RK1A} = -\mathcal{C}_{10}^{RK1A} = \frac{\pi V_{cb} V_{cs}^* (\lambda_{22}^L)^2}{\sqrt{2} G_F V_{ib} V_{is}^* \alpha M_{U_1}^2}. \quad (39)$$

The contribution to the $B_s - \bar{B}_s$ mixing coefficient is

$$\mathcal{C}_{\text{box}}^{U_1} = \frac{|V_{cb}|^2 |V_{cs}|^2 (\lambda_{22}^L)^4}{8\pi^2 M_{U_1}^2}. \quad (40)$$

The dominant decay modes of U_1 in this case are $U_1 \rightarrow c\bar{v}$ and $U_1 \rightarrow s\mu^+$ with almost 50% BR each.

I. Scenario RK1B

Only λ_{32}^L is nonzero. The interaction Lagrangian is given by,

$$\mathcal{L} \supset \lambda_{32}^L [\bar{t}_L \gamma_\mu \nu_L + (V_{id}^* \bar{d}_L + V_{is}^* \bar{s}_L + V_{ib}^* \bar{b}_L) \gamma_\mu \mu_L] U_1^\mu. \quad (41)$$

The relevant Wilson coefficients are given by

$$\mathcal{C}_9^{RK1B} = -\mathcal{C}_{10}^{RK1B} = \frac{\pi}{\sqrt{2} G_F \alpha} \frac{(\lambda_{32}^L)^2}{M_{U_1}^2}, \quad (42)$$

and the contribution to the $B_s - \bar{B}_s$ mixing coefficient is given as

$$\mathcal{C}_{\text{box}}^{U_1} = \frac{|V_{ib}|^2 |V_{is}|^2 (\lambda_{32}^L)^4}{8\pi^2 M_{U_1}^2}. \quad (43)$$

Here, the $\bar{s}\mu U_1$ coupling is V_{is}^* -suppressed. The coupling λ_{32}^L alone, however, cannot explain the $R_K^{(*)}$ anomalies. From Table III we see that the anomalies need a negative \mathcal{C}_9 , whereas the rhs of Eq. (42) is always positive (even if we consider a complex λ_{32}^L). The dominant decay modes of U_1 in this case are $U_1 \rightarrow t\bar{v}$ and $U_1 \rightarrow b\mu^+$, and they share almost 50% BR each.

J. Scenario RK1C

In this scenario, we assume only λ_{22}^R to be nonzero. The interaction Lagrangian is given by

TABLE III. Global fits of relevant combinations of Wilson coefficients in $b \rightarrow s\mu\mu$ observables [104,105,109].

Combinations	Best fit	1σ	2σ	Corresponding scenarios
$\mathcal{C}_9^{U_1} = -\mathcal{C}_{10}^{U_1}$	-0.44	[-0.52, -0.37]	[-0.60, -0.29]	RK1A, RK1B, RK2A
$\mathcal{C}_S^{U_1} = -\mathcal{C}_P^{U_1}$	-0.0252	[-0.0378, -0.126]	[-0.0588, -0.0042]	RK2B
$\mathcal{C}'_9^{U_1} = \mathcal{C}'_{10}^{U_1}$	+0.06	[-0.18, +0.30]	[-0.42, +0.55]	RK1C, RK1D, RK2D
$\mathcal{C}'_S^{U_1} = \mathcal{C}'_P^{U_1}$	-0.0252	[-0.0378, -0.126]	[-0.0588, -0.0042]	RK2C

$$\mathcal{L} \supset \lambda_{22}^R [(V_{cd}\bar{d}_R + V_{cs}\bar{s}_R + V_{cb}\bar{b}_R)\gamma_\mu\mu_R]U_1^\mu. \quad (44)$$

The nonzero Wilson coefficients from Eq. (37) are

$$\mathcal{C}_9^{iRK1C} = \mathcal{C}_{10}^{iRK1C} = \frac{\pi V_{cb}^* V_{cs}}{\sqrt{2}G_F V_{tb} V_{ts}^* \alpha} \frac{(\lambda_{22}^R)^2}{M_{U_1}^2}, \quad (45)$$

and the contribution to the $B_s - \bar{B}_s$ mixing coefficient is

$$\mathcal{C}_{\text{box}}^{U_1} = \frac{|V_{cb}|^2 |V_{cs}|^2 (\lambda_{22}^R)^4}{8\pi^2 M_{U_1}^2}. \quad (46)$$

Here, the $\bar{b}\mu U_1$ coupling is V_{cb}^* suppressed. In this scenario, the $U_1 \rightarrow s\mu^+$ decay mode has almost 100% BR.

K. Scenario RK1D

We assume λ_{32}^R to be nonzero and the rest of the couplings to be SM-like. The interaction Lagrangian is given by

$$\mathcal{L} \supset \lambda_{32}^R [(V_{td}\bar{d}_R + V_{ts}\bar{s}_R + V_{tb}\bar{b}_R)\gamma_\mu\mu_R]U_1^\mu, \quad (47)$$

where the $\bar{s}\mu U_1$ coupling is V_{ts} suppressed. The nonzero Wilson coefficients are

$$\mathcal{C}_9^{iRK1D} = \mathcal{C}_{10}^{iRK1D} = \frac{\pi V_{tb}^* V_{ts}}{\sqrt{2}G_F V_{tb} V_{ts}^* \alpha} \frac{(\lambda_{32}^R)^2}{M_{U_1}^2}. \quad (48)$$

In this scenario, the $U_1 \rightarrow b\mu^+$ decay mode is dominant with almost 100% BR. The contribution to the $B_s - \bar{B}_s$ mixing coefficient is given as

$$\mathcal{C}_{\text{box}}^{U_1} = \frac{|V_{tb}|^2 |V_{ts}|^2 (\lambda_{32}^R)^4}{8\pi^2 M_{U_1}^2}. \quad (49)$$

L. Scenario RK2A

In this scenario, two couplings, namely, λ_{22}^L and λ_{32}^L , are nonzero. The interaction Lagrangian is given by

$$\mathcal{L} \supset [\lambda_{22}^L (\bar{c}_L \gamma_\mu \nu_L + \bar{s}_L \gamma_\mu \mu_L) + \lambda_{32}^L (\bar{t}_L \gamma_\mu \nu_L + \bar{b}_L \gamma_\mu \mu_L)]U_1^\mu. \quad (50)$$

Here, we have not shown the CKM-suppressed couplings. The Wilson coefficients getting the dominant contributions are

$$\mathcal{C}_9^{RK2A} = -\mathcal{C}_{10}^{RK2A} \approx \frac{\pi}{\sqrt{2}G_F V_{tb} V_{ts}^* \alpha} \frac{\lambda_{22}^L \lambda_{32}^L}{M_{U_1}^2}. \quad (51)$$

The contribution to the $B_s - \bar{B}_s$ mixing coefficient is

$$\mathcal{C}_{\text{box}}^{U_1} = \frac{(\lambda_{22}^L)^2 (\lambda_{32}^L)^2}{8\pi^2 M_{U_1}^2}. \quad (52)$$

In this scenario, the dominant decay modes for U_1 are $b\mu^+$, $s\mu^+$, $c\bar{\nu}$, and $t\bar{\nu}$.

M. Scenario RK2B

In this scenario, only λ_{22}^L and λ_{32}^R are nonzero. The interaction Lagrangian is given by

$$\mathcal{L} \supset [\lambda_{22}^L (\bar{c}_L \gamma_\mu \nu_L + \bar{s}_L \gamma_\mu \mu_L) + \lambda_{32}^R \bar{b}_R \gamma_\mu \mu_R]U_1^\mu. \quad (53)$$

Here, once again, the CKM-suppressed couplings are ignored. The Wilson coefficients getting the dominant contributions are

$$-\mathcal{C}_P^{RK2B} = \mathcal{C}_S^{RK2B} \approx \frac{\sqrt{2}\pi}{G_F V_{tb} V_{ts}^* \alpha} \frac{\lambda_{22}^L \lambda_{32}^R}{M_{U_1}^2}. \quad (54)$$

For this scenario, $B_s - \bar{B}_s$ mixing is not relevant. The dominant decay modes of U_1 are $b\mu^+$, $s\mu^+$, and $c\bar{\nu}$.

N. Scenario RK2C

Only λ_{22}^R and λ_{32}^L are nonzero. Ignoring the CKM-suppressed couplings, we get the following interaction Lagrangian:

$$\mathcal{L} \supset [\lambda_{22}^R \bar{s}_R \gamma_\mu \mu_R + \lambda_{32}^L (\bar{t}_L \gamma_\mu \nu_L + \bar{b}_L \gamma_\mu \mu_L)]U_1^\mu. \quad (55)$$

The Wilson coefficients getting the dominant contributions are

$$\mathcal{C}_P^{iRK2C} = \mathcal{C}_S^{iRK2C} \approx \frac{\sqrt{2}\pi}{G_F V_{tb} V_{ts}^* \alpha} \frac{\lambda_{22}^R \lambda_{32}^L}{M_{U_1}^2}. \quad (56)$$

In this case also $B_s - \bar{B}_s$ mixing is not relevant. The dominant decay modes of U_1 are $b\mu^+$, $s\mu^+$, and $t\bar{\nu}$.

O. Scenario RK2D

Only λ_{22}^R and λ_{32}^R are nonzero. Ignoring the CKM-suppressed couplings, we get

$$\mathcal{L} \supset (\lambda_{22}^R \bar{s}_R \gamma_\mu \mu_R + \lambda_{32}^R \bar{b}_R \gamma_\mu \mu_R)U_1^\mu. \quad (57)$$

The Wilson coefficients getting the dominant contributions are

$$\mathcal{C}_9^{iRK2D} = \mathcal{C}_{10}^{iRK2D} \approx \frac{\pi}{\sqrt{2}G_F V_{tb} V_{ts}^* \alpha} \frac{\lambda_{22}^R \lambda_{32}^R}{M_{U_1}^2}. \quad (58)$$

The contribution to the $B_s - \bar{B}_s$ mixing coefficient is given as

TABLE IV. Summary of the coupling combinations that contribute to the $R_{D^{(*)}}$ and $R_{K^{(*)}}$ observables in different one-, two-, and multi-coupling scenarios.

$R_{D^{(*)}}$ scenarios	$\lambda_{c\nu}^L$	$\lambda_{b\tau}^L$	$\lambda_{b\tau}^R$	$R_{K^{(*)}}$ scenarios	$\lambda_{s\mu}^L$	$\lambda_{b\mu}^L$	$\lambda_{s\mu}^R$	$\lambda_{b\mu}^R$
RD1A	λ_{23}^L	$V_{cb}^* \lambda_{23}^L$	\dots	RK1A	$V_{cs}^* \lambda_{22}^L$	$V_{cb}^* \lambda_{22}^L$	\dots	\dots
RD1B	$V_{cb} \lambda_{33}^L$	λ_{33}^L	\dots	RK1B	$V_{ts}^* \lambda_{32}^L$	$V_{tb}^* \lambda_{32}^L$	\dots	\dots
				RK1C	\dots	\dots	$V_{cs} \lambda_{22}^R$	$V_{cb} \lambda_{22}^R$
				RK1D	\dots	\dots	$V_{ts} \lambda_{32}^R$	$V_{tb} \lambda_{32}^R$
RD2A	$V_{cs} \lambda_{23}^L + V_{cb} \lambda_{33}^L$	λ_{33}^L	\dots	RK2A	λ_{22}^L	λ_{32}^L	\dots	\dots
RD2B	$V_{cs} \lambda_{23}^L$	\dots	λ_{33}^R	RK2B	λ_{22}^L	\dots	\dots	λ_{32}^R
				RK2C	\dots	λ_{32}^L	λ_{22}^R	\dots
				RK2D	\dots	\dots	λ_{22}^R	λ_{32}^R
RD3	$V_{cb} \lambda_{33}^L + V_{cs} \lambda_{23}^L$	λ_{33}^L	λ_{33}^R	RK4	λ_{22}^L	λ_{32}^L	λ_{22}^R	λ_{32}^R

$$\mathcal{C}_{\text{box}}^{U_1} = \frac{(\lambda_{22}^R)^2 (\lambda_{32}^R)^2}{8\pi^2 M_{U_1}^2}. \quad (59)$$

The dominant decay modes of U_1 are $b\mu^+$ and $s\mu^+$.

P. Scenario RK4

All couplings are nonzero. In this scenario, the interaction Lagrangian is given by

$$\mathcal{L} \supset [\lambda_{22}^L (\bar{c}_L \gamma_\mu \nu_L + \bar{s}_L \gamma_\mu \mu_L) + \lambda_{32}^L (\bar{t}_L \gamma_\mu \nu_L + \bar{b}_L \gamma_\mu \mu_L) + \lambda_{22}^R \bar{s}_R \gamma_\mu \mu_R + \lambda_{32}^R \bar{b}_R \gamma_\mu \mu_R] U_1^\mu, \quad (60)$$

and the dominant contributions to the Wilson coefficients can be read from Eq. (37). The main decay modes of U_1 are $c\bar{\nu}$, $t\bar{\nu}$, $s\mu^+$, and $b\mu^+$.

Our selection of scenarios motivated by the $R_K^{(*)}$ anomalies is not exhaustive. For example, we do not consider any three-coupling scenarios. (One can define RK3X scenarios by taking combinations of three couplings at a time for completeness. We, however, skip the three-coupling $R_{K^{(*)}}$ scenarios since they would not add anything significant to our study.) The single-coupling scenarios can be thought of as templates that can help us read bounds on scenarios where more than one couplings are nonzero [63,81]. In Table III, we show the relevant global fits for the one- and two-coupling scenarios. We have summarized the couplings that contribute to the $R_{D^{(*)}}$ and $R_{K^{(*)}}$ observables in different scenarios in Table IV.

As mentioned earlier, one of the reasons for considering the $R_{D^{(*)}}$ and $R_{K^{(*)}}$ scenarios is that they can have different signatures at the LHC. We are now in a position to illustrate that point further. Let us consider the first two $R_{D^{(*)}}$ -motivated one-coupling scenarios—Scenario RD1A and Scenario RD1B. In both cases, \mathcal{C}_{V_L} receives a nonzero contribution proportional to the square of an unknown new coupling (either λ_{23}^L or λ_{33}^L). Hence, from an effective theory perspective, these two look almost the same. However, the

dominant decay modes of U_1 in these two scenarios are different—in the first one, they are $U_1 \rightarrow c\nu$ and $U_1 \rightarrow s\tau$, whereas in the second one, they are $U_1 \rightarrow t\nu$ and $U_1 \rightarrow b\tau$.³ As a result, a U_1 can produce $t + \cancel{E}_T$ or $\tau + b$ signatures in the second scenario, as opposed to the jet + \cancel{E}_T or $\tau + \text{jet}$ signatures in the first one. Not only that, in the first scenario, a U_1 can be produced via c - or s -quark-initiated processes, as compared to the b -quark-initiated processes in the second one. Hence, in these two scenarios, U_1 would have different single production processes. Moreover, since the b -quark parton distribution function (PDF) is smaller than the second-generation ones, U_1 production cross sections would be higher in Scenario RD1A than those in Scenario RD1B. Hence, one needs to analyze the LHC bounds for the scenarios differently.

III. PRODUCTION MODES AND DECAYS

We now explore the possible LHC signatures of the minimal scenarios with only one free coupling and the next-to-minimal scenarios with more than one nonzero couplings we constructed in the previous section. There are different ways to produce U_1 at the LHC (see Fig. 3)—resonantly (through pair and single productions) and nonresonantly (through t -channel U_1 exchange). Below, we briefly discuss various production channels and the subsequent decay modes of U_1 that can arise in the flavor-motivated scenarios. We also discuss how different production modes with similar final states can contribute to the exclusion limits.

A. Pair production

We have classified the $R_{D^{(*)}}$ scenarios with the three free couplings, λ_{23}^L , λ_{33}^L , and λ_{33}^R . In Scenario RD1A (where only

³From here on, unless necessary, we do not distinguish between particles and their antiparticles as it is not important for the LHC analysis.

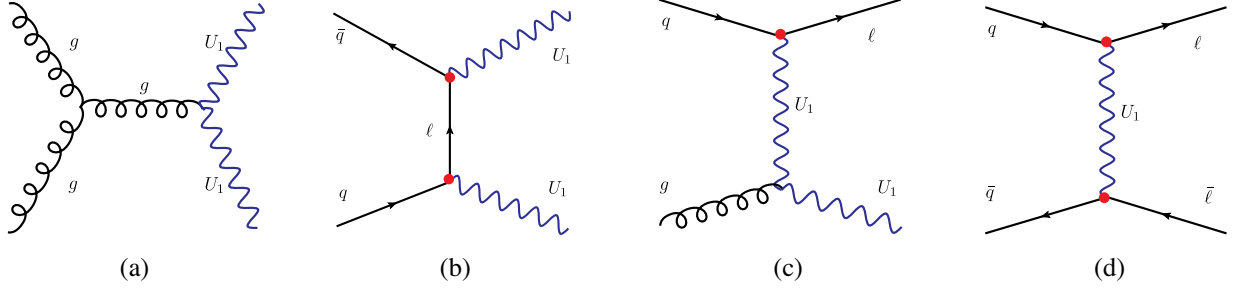


FIG. 3. Representative Feynman diagrams for various U_1 production processes: (a) gluon-initiated pair production, (b) quark-initiated pair production, (c) single production, and (d) t -channel (nonresonant) production. The $q\ell U_1$ vertices (λ) are marked with red color.

λ_{23}^L is nonzero), $U_1 \rightarrow s\tau$ and $U_1 \rightarrow c\nu$ are the main decay modes of U_1 with roughly equal (about 50%) BRs. In this case the pair production of U_1 leads to the following final states (we ignore the CKM-suppressed effective couplings in the discussions on the LHC phenomenology of U_1 as they do not play any important role):

$$pp \rightarrow \left\{ \begin{array}{l} U_1 U_1 \rightarrow s\tau s\tau \equiv \tau\tau + 2j \\ U_1 U_1 \rightarrow s\tau c\nu \equiv \tau + \cancel{E}_T + 2j \\ U_1 U_1 \rightarrow c\nu c\nu \equiv \cancel{E}_T + 2j \end{array} \right\}, \quad (61)$$

where j denotes a light jet or a b -jet. Among the three channels, the second one (i.e., $\tau + \cancel{E}_T + 2j$) has almost two times the cross section of the first or the third (a factor of 2 comes from combinatorics), but due to the presence of missing energy, it is not fully reconstructable (or, is difficult to reconstruct). As a result, both the first and second channels have comparable sensitivities. However, the sensitivity of the third channel, $\cancel{E}_T + 2j$, is very poor because of the two neutrinos in the final state. So far, these channels with cross-generation couplings have not been used in any LQ search at the LHC.

In Scenario RD1B (where only λ_{33}^L is nonzero), the pair production of U_1 mostly leads to the following final states:

$$pp \rightarrow \left\{ \begin{array}{l} U_1 U_1 \rightarrow b\tau b\tau \equiv \tau\tau + 2j \\ U_1 U_1 \rightarrow b\tau t\nu \equiv \tau + \cancel{E}_T + j_t + j \\ U_1 U_1 \rightarrow t\nu t\nu \equiv \cancel{E}_T + 2j_t \end{array} \right\}. \quad (62)$$

Here, j_t represents a fat-jet originating from a top quark decaying hadronically (one can also consider the top quark's leptonic decay modes with a lower cross section). It is possible to tag the (boosted) top-jets with sophisticated jet-substructure techniques and thus improve the second and third channels' prospects. The symmetric $\cancel{E}_T + 2j_t$ channel has been considered in Refs. [58,110]. The asymmetric channel, the one with single τ , one top-jet, and missing energy ($\tau + \cancel{E}_T + j_t + b$), has started receiving attention only very recently [88]. Due to the factor of 2 coming from combinatorics, this channel has a bigger cross

section. Hence, its unique final state might act as a smoking-gun signature for this type of scenario (i.e., ones with non-negligible λ_{33}^L).

If only λ_{33}^R is nonzero, U_1 cannot resolve the $R_{D^{(*)}}$ anomalies anymore as it is not possible to generate the necessary couplings in that case. Here, U_1 entirely decays through the $U_1 \rightarrow b\tau$ mode and contributes to the $b\tau b\tau \equiv \tau\tau + 2j$ final state [85].

When two or more couplings are nonzero simultaneously (Scenario RD2A, Scenario RD2B, and Scenario RD3) with comparable strengths, numerous possibilities arise (Reference [63] discusses this in the context of scalar LQ searches). It is then possible to have all the final states shown in Eqs. (61) and (62). One can have more asymmetric channels like $pp \rightarrow U_1 U_1 \rightarrow s\tau b\tau$ etc. The strength of any particular channel would depend on the couplings involved in production (if we do not ignore the small t -channel lepton exchange) as well as the BRs involved (the dependence of the pair production signal on multiple couplings is made explicit in Appendix A).

The $R_{K^{(*)}}$ scenarios have similar signatures with muons in the final states. When only λ_{22} is nonzero (Scenario RK1A), we can easily obtain the possible final states by replacing $\tau \rightarrow \mu$ in Eq. (61). In Scenario RK1B, the possible final states are obtained by replacing $\tau \rightarrow \mu$ in Eq. (62). In Scenario RK1C, the BR of the $U_1 \rightarrow s\mu$ decay is 100% leading to the process, $U_1 U_1 \rightarrow s\mu s\mu \equiv \mu\mu + 2j$. Similarly, in Scenario RK1D, the BR of the $U_1 \rightarrow b\mu$ decay is 100% leading to the same two-muon + two-jet final states through the $U_1 U_1 \rightarrow b\mu b\mu \equiv \mu\mu + 2j$ process. Like the $R_{D^{(*)}}$ scenarios with more than one nonzero couplings, these scenarios also lead to numerous interesting possibilities [63]. The LHC is yet to perform searches for LQs in most of the asymmetric channels and some of the symmetric channels.

In Table V, we have summarized the possible final states from U_1 pair production and the fraction of U_1 pairs producing the final states in the one- and two-coupling scenarios. The fractions depend on combinatorics and the relevant U_1 BRs. (Here, we have ignored the possible minor correction due the mass differences between different final states, i.e., assumed all final state particles are

TABLE V. Effect of branching ratios on different final states generated from the $pp \rightarrow U_1 U_1$ process in various one and two-coupling scenarios. Here, we show the possible final states and the fraction of U_1 pairs producing them. One multiplies the pair production cross section with the fractions shown in the table to estimate its contribution to various channels in the narrow width approximation. Here, $0 \leq \xi \leq \frac{1}{2}$ is a free parameter. We have ignored the mass differences among the daughter particles.

Nonzero couplings	Signatures					
	$\tau\tau + 2j$	$\tau + \cancel{E}_T + 2j$	$\cancel{E}_T + 2j$	$\tau + \cancel{E}_T + j_t + j$	$\cancel{E}_T + 2j_t$	$\cancel{E}_T + j_t + j$
λ_{23}^L (Scenario RD1A)	0.25	0.50	0.25
λ_{33}^L (Scenario RD1B)	0.25	0.50	0.25	...
λ_{33}^R	1.00
$\lambda_{23}^L, \lambda_{33}^L$ (Scenario RD2A)	0.25	ξ	ξ^2	$\frac{1}{2} - \xi$	$(\frac{1}{2} - \xi)^2$	$2\xi(\frac{1}{2} - \xi)$
$\lambda_{23}^L, \lambda_{33}^R$ (Scenario RD2B)	$(\frac{1}{2} + \xi)^2$	$2(\frac{1}{4} - \xi^2)$	$(\frac{1}{2} - \xi)^2$
	$\mu\mu + 2j$	$\mu + \cancel{E}_T + 2j$	$\cancel{E}_T + 2j$	$\mu + \cancel{E}_T + j_t + j$	$\cancel{E}_T + 2j_t$	$\cancel{E}_T + j_t + j$
λ_{22}^L (Scenario RK1A)	0.25	0.50	0.25
λ_{32}^L (Scenario RK1B)	0.25	0.50	0.25	...
λ_{22}^R (Scenario RK1C)	1.00
λ_{32}^R (Scenario RK1D)	1.00
$\lambda_{22}^L, \lambda_{32}^L$ (Scenario RK2A)	0.25	ξ	ξ^2	$\frac{1}{2} - \xi$	$(\frac{1}{2} - \xi)^2$	$2\xi(\frac{1}{2} - \xi)$
$\lambda_{22}^L, \lambda_{32}^R$ (Scenario RK2B)	$(\frac{1}{2} + \xi)^2$	$2(\frac{1}{4} - \xi^2)$	$(\frac{1}{2} - \xi)^2$
$\lambda_{22}^R, \lambda_{32}^L$ (Scenario RK2C)	$(\frac{1}{2} + \xi)^2$	$2(\frac{1}{4} - \xi^2)$	$(\frac{1}{2} - \xi)^2$...
$\lambda_{22}^R, \lambda_{32}^R$ (Scenario RK2D)	1.00

much lighter than U_1 .) For example, in Scenario RD1A, since $\beta(U_1 \rightarrow s\tau) \approx \beta(U_1 \rightarrow c\nu) \approx 50\%$, only 25% of the produced U_1 pairs would decay to either $\tau\tau + 2j$ or $\cancel{E}_T + 2j$, whereas, as explained above, 50% of them would decay to the $\tau + \cancel{E}_T + 2j$ final state. Interestingly, we see that even in some two-coupling scenarios the fractions corresponding to the $\tau\tau/\mu\mu + 2j$ final states are constant irrespective of the relative magnitudes of the couplings—for example, it is 25% in Scenario RD2A or 100% in Scenario RK2D. This is interesting, because in the presence of two nonzero couplings, one normally expects the fraction corresponding to a particular final state to depend on their relative strengths. This, of course, happens because we sum over the possible flavors of the jets. Moreover, we show that it is possible to parametrize all final states with just one free parameter (ξ). Such simple parametrizations could guide us in future U_1 searches at the LHC.

Note that the model dependence of the pair production of U_1 appears in two places. One occurs through the free parameter κ present in the kinetic terms ($ig_s \kappa U_{1\mu}^\dagger T^a U_{1\nu} G^{a\mu\nu}$) [84,92]. The pair production cross section depends on κ . The other occurs in the contribution of the t -channel lepton/neutrino exchange. The amplitudes of these diagrams grow as λ^2 , and the cross section grows as λ^4 . Although the λ dependence of the pair production is negligible for small λ values, it can become significant for larger couplings. As we see later, the pair production channels produce a relatively minor contribution to the final exclusion limits. Therefore, we take a benchmark value for κ by setting $\kappa = 0$ in our

analysis. However, we keep the λ -dependent terms in the pair production contributions (see Appendix A).

B. Single production

In the single-production channels, a U_1 is produced in association with other SM particles. There are two types of single productions of our interest: (a) where a U_1 is produced in association with a lepton, i.e., $U_1\mu$, $U_1\tau$ or $U_1\nu$ and (b) where a U_1 is produced with a lepton and a jet, i.e., $U_1\mu j$, $U_1\tau j$ or $U_1\nu j$. One has to be careful while computing the second type of process as the set of Feynman diagrams for them might overlap with the pair production ones when the lepton-jet pair originates in a LQ decay. We keep the two types of single production contributions in our analysis by carefully avoiding any double counting with the pair production contribution [111–113]. Single productions of U_1 are fully model-dependent processes; they depend on the coupling λ as well as κ [84]. Like the pair production, the single production processes can also be categorized into symmetric and asymmetric channels [63]. In Scenario RD1A, we have the following single production channels:

$$pp \rightarrow \left\{ \begin{array}{l} U_1\tau + U_1\tau j \rightarrow (s\tau)\tau + (s\tau)\tau j \equiv \tau\tau + nj \\ U_1\nu + U_1\nu j \rightarrow (c\nu)\nu + (c\nu)\nu j \equiv \cancel{E}_T + nj \\ U_1\tau + U_1\tau j \rightarrow (c\nu)\tau + (c\nu)\tau j \equiv \tau + \cancel{E}_T + nj \\ U_1\nu + U_1\nu j \rightarrow (s\tau)\nu + (s\tau)\nu j \equiv \tau + \cancel{E}_T + nj \end{array} \right\}. \quad (63)$$

Notice that the single production processes produce similar final states as the pair production. In the above equation, the first and the second channels are symmetric, whereas the third and the fourth are asymmetric. In the $\tau + \cancel{E}_T + nj$ final state, both $pp \rightarrow U_1\tau + U_1\tau j$ and $pp \rightarrow U_1\nu + U_1\nu j$ contribute. This channel also has not been considered for LQ searches so far. Scenario RD1B is very similar to Scenario RD1A and gives the

$$pp \rightarrow \left\{ \begin{array}{l} U_1\mu + U_1\mu j \rightarrow (b\mu)\mu + (b\mu)\mu j \equiv \mu\mu + nj \\ U_1\mu + U_1\mu j \rightarrow (t\nu)\mu + (t\nu)\mu j \equiv \mu + \cancel{E}_T + j_t + nj \\ U_1\nu + U_1\nu j \rightarrow (b\mu)\nu + (b\mu)\nu j \equiv \mu + \cancel{E}_T + nj \\ U_1\nu + U_1\nu j \rightarrow (t\nu)\nu + (t\nu)\nu j \equiv \cancel{E}_T + j_t + nj \end{array} \right\}. \quad (64)$$

These final states can also come from pair production in Scenario RK1B. In Scenario RK1C, the $U_1 \rightarrow s\mu$ decay has 100% BR, and it leads to the process $U_1\mu + U_1\mu j \rightarrow (s\mu)\mu + (s\mu)\mu j \equiv \mu\mu + nj$. In Scenario RK1D, the $U_1 \rightarrow b\mu$ decay mode has 100% BR. It leads to the process $U_1\mu + U_1\mu j \rightarrow (b\mu)\mu + (b\mu)\mu j \equiv \mu\mu + nj$.

C. Nonresonant production and interference

A U_1 can be exchanged in the t -channel and give rise to both dilepton and lepton + missing-energy final states [see e.g., Fig. 3(d)]. As the cross sections of the nonresonant production grows as λ^4 , this channel becomes important for large values of the new couplings. Especially when the mass of the U_1 is large, the nonresonant production contributes more than the resonant pair and single productions. There is a possibility of large interference of the nonresonant processes with the SM backgrounds like

same final states if we treat the b -jet as a light jet. If only λ_{33}^R is nonzero, U_1 decays only to $b\tau$. Thus this scenario only leads to the $(b\tau)\tau + (b\tau)\tau j \equiv \tau\tau + nj$ final state.

The possible final states in case of Scenario RK1A can be obtained by replacing $\tau \rightarrow \mu$ in Eq. (63). In Scenario RK1B, we have some interesting signatures from boosted top quarks in the final states,

$pp \rightarrow \gamma/Z(W) \rightarrow \ell\ell(\ell + \cancel{E}_T)$. The interference contribution grows as λ^2 , but the contribution can be significant due to the large SM background. For U_1 , the interference is destructive in nature. However, depending on the parameter/kinematic region we consider, the cross section of the exclusive $pp \rightarrow \ell\ell(\ell + \cancel{E}_T)$ process can be bigger or smaller than the SM-only contribution [57] because the total nonresonant contribution, including the term proportional to λ^4 and the destructive λ^2 term, can be both positive or negative.

In Fig. 4, we show the parton-level cross sections of various production modes of U_1 as a function of M_{U_1} . In Figs. 4(a) and 4(b) the cross sections have been obtained by setting $\kappa = 0$ and the new couplings, $\lambda_{23}^L = 1$ and $\lambda_{22}^L = 1$ respectively. The pair production cross section is the same in both figures as it is insensitive to the λ couplings. As expected, the single production cross sections are more

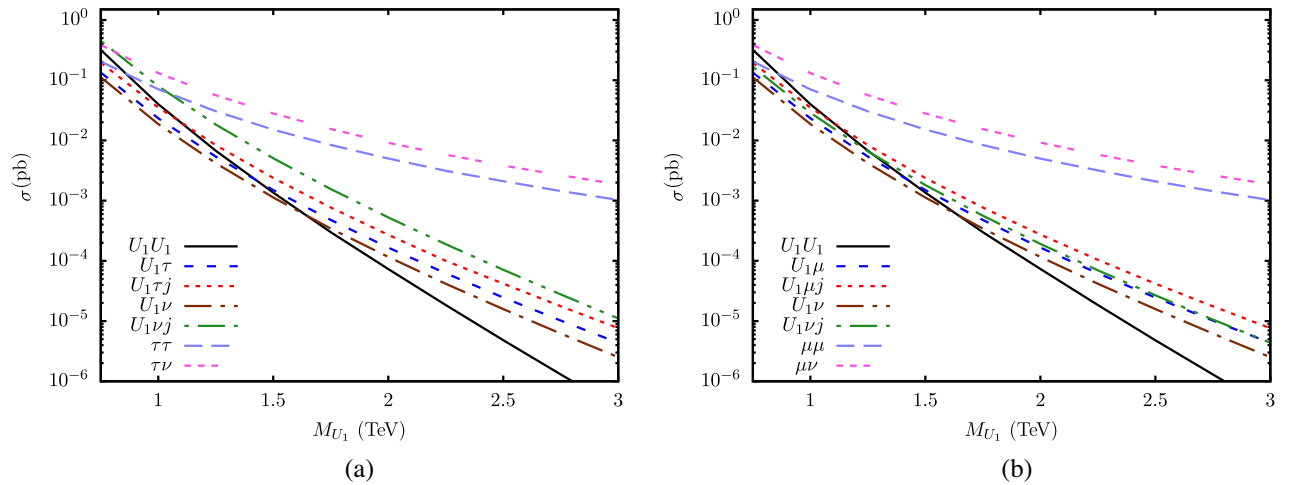


FIG. 4. Parton-level cross sections of various production modes of U_1 LQ as functions of M_{U_1} . These cross sections are computed at the 13 TeV LHC for benchmark couplings, $\lambda_{23}^L = 1$ (left) and $\lambda_{22}^L = 1$ (right) with $\kappa = 0$. Here, j stands for all light jets including the b -jet. A basic generation-level cut, $p_T > 20$ GeV, is applied on the jets and leptons.

significant at higher mass values. Processes like $U_1\tau j$, $U_1\mu j$, $U_1\nu j$ are generated after ensuring that no more than one onshell LQ contributes to the cross section to avoid contamination from the pair production process. The nonresonant LQ production cross section does not depend very strongly on the LQ mass. With nonzero λ_{23}^L and λ_{22}^L , we now have the possibility of producing U_1 (that couples to the third-generation fermions) through charm- and/or strange-initiated processes at the LHC.

There are some phenomenological consequences of having more than one coupling. The presence of multiple couplings affects the BRs. For example, we see from Table V that BRs for one-coupling scenarios are different from those in two coupling ones. Then, different single and nonresonant production (including its interference with the SM background) processes may or may not become significant depending on the strength of various couplings. All these can significantly affect the exclusion limits.

IV. RECAST OF DILEPTON DATA

From the different production mechanisms of U_1 discussed in the previous section, it is evident that pair, single, and nonresonant productions can give rise to dilepton ($\ell\ell + jets$) and/or monolepton plus missing-energy, $\ell + \cancel{E}_T + jets$, signatures. However, as pointed out in Ref. [81] for S_1 LQ, the bounds on the LQ model parameter space from the dilepton resonance search data are more stringent. Therefore, apart from the direct search bounds, we rely only on the resonant dilepton searches ($pp \rightarrow Z' \rightarrow \ell\ell$) [82,83] and recast the bounds in terms of U_1 parameters for various scenarios. Note that the number of jets are not restricted in those searches, and hence all production modes of U_1 with $\ell\ell + jets$ final states would contribute in the exclusion limits. As shown in [81], the interference of the t -channel U_1 exchange process with the SM background play the leading role in determining the exclusion limits. However, pair, single, and nonresonant productions also contribute non-negligibly, especially in the lower mass region. Since, the kinematics of different U_1 contributions to the $\ell\ell + jets$ channel are different from those of the resonant dilepton production ($pp \rightarrow Z' \rightarrow \ell\ell$), recasting is nontrivial, especially when multiple new couplings are present. Possible interference among different signal processes complicate the recasting further. We systematically take care of all these factors in our analysis. We explain our method in Appendix A.

A. ATLAS $\tau\tau$ search

The ATLAS Collaboration searched for a heavy particle decaying to two taus at the 13 TeV LHC with 139 fb^{-1} integrated luminosity [82]. The analysis comprised events categorized on the basis of two modes of τ decays. In the first, one has both τ 's decaying hadronically ($\tau_{had}\tau_{had}$).

In the second, one tau decays hadronically and the other leptonically ($\tau_{had}\tau_{lep}$). We provide an outline of the basic event selection criteria for the $\tau\tau$ channel.

(i) The $\tau_{had}\tau_{had}$ channel has at least two hadronically decaying τ 's with no additional electrons or muons,

two τ_{had} 's with $p_T > 65 \text{ GeV}$. They should be oppositely charged and separated in the azimuthal plane by $|\Delta\phi(p_T^{\tau_1}, p_T^{\tau_2})| > 2.7 \text{ rad}$.

p_T of leading τ must be $> 85 \text{ GeV}$.

(ii) The $\tau_{lep}\tau_{had}$ channel has one τ_{had} and only one $\ell = e$ or μ such that

the hadronic τ has $p_T > 25 \text{ GeV}$ and $|\eta(\tau_{had})| < 2.5$ (excluding $1.37 < |\eta| < 1.52$),

if $\ell = e$, then $|\eta| < 2.47$ (excluding $1.37 < |\eta| < 1.52$) and if $\ell = \mu$ then $|\eta| < 2.5$,

the lepton has $p_T(\ell) > 30 \text{ GeV}$ with azimuthal separation from the τ_{had} , $|\Delta\phi(p_T^\ell, p_T^{\tau_{had}})| > 2.4$.

the transverse mass on the selected lepton and missing transverse momentum, $m_T(p_T^\ell, \cancel{E}_T) > 40 \text{ GeV}$.

If $\ell = e$, to reduce the background from $Z \rightarrow ee$ events with an invariant mass for $\tau - \ell$ pair between 80 GeV and 110 GeV are rejected.

The transverse mass is defined as

$$m_T(p_T^A, p_T^B) = \sqrt{2p_T^A p_T^B \{1 - \cos \Delta\phi(p_T^A, p_T^B)\}}. \quad (65)$$

The analysis also make use of the total transverse mass defined as

$$m_T^{\text{tot}}(\tau_1, \tau_2, \cancel{E}_T) = \sqrt{m_T^2(p_T^{\tau_1}, p_T^{\tau_2}) + m_T^2(p_T^{\tau_1}, \cancel{E}_T) + m_T^2(p_T^{\tau_2}, \cancel{E}_T)}. \quad (66)$$

Here, τ_2 in the $\tau_{lep}\tau_{had}$ channel represents the lepton. We use the distribution of the observed and the SM events with respect to m_T^{tot} presented in the analysis.

B. CMS $\mu\mu$ search

A search for nonresonant excesses in the dilepton channel was performed by the CMS experiment at a centre-of-mass energy of 13 TeV corresponding to a integrated luminosity of 140 fb^{-1} [83]. The event selection criteria that we use in our analysis can be summarised as

(i) In the dimuon channel, the requirement is that both of the muons must have $|\eta| < 2.4$ and $p_T > 53 \text{ GeV}$.

The invariant mass of the muon pair is $m_{\mu\mu} > 150 \text{ GeV}$.

We use the distribution of the observed and the SM events with respect to the invariant mass of the muon pair, $m_{\mu\mu}$ to extract bounds.

We implement the above cuts in our analysis codes after validating them with the efficiencies given in the experimental papers. As explained in Ref. [81], we generated

TABLE VI. The table displays the cross section (σ) in fb, efficiency (ϵ) in %, and number of events (\mathcal{N}) surviving the cuts applied in the dilepton searches from various production processes. The superscripts are explained in Appendix A. The negative signs in the interference contributions signify destructive interference.

Mass(TeV)	Pair production			Single production			t -channel LQ			Interference		
	σ^p	ϵ^p	\mathcal{N}^p	σ^s	ϵ^s	\mathcal{N}^s	σ^{nr4}	ϵ^{nr4}	\mathcal{N}^{nr4}	σ^{nr2}	ϵ^{nr2}	\mathcal{N}^{nr2}
Contribution to $\tau\tau$ signal [82]												
$\lambda_{23}^L = 1$ (Scenario RD1A)												
1.0	40.87	2.33	8.59	58.80	3.30	35.07	70.57	7.22	183.33	-232.63	3.17	-266.21
1.5	1.39	1.50	0.19	3.91	2.74	1.93	14.94	7.00	37.77	-104.31	3.34	-125.62
2.0	0.08	1.01	0.01	0.44	2.50	0.20	5.04	7.25	13.19	-58.79	3.28	-69.57
$\lambda_{33}^L = 1$ (Scenario RD1B)												
1.0	35.67	1.69	5.43	29.00	2.57	13.46	20.20	6.21	45.26	-75.02	3.08	-83.41
1.5	1.17	1.09	0.11	1.72	2.16	0.67	4.31	6.22	9.68	-33.62	2.88	-33.01
2.0	0.06	0.81	0.00	0.17	1.98	0.06	1.39	6.27	3.15	-18.97	2.88	-19.71
$\lambda_{33}^R = 1$												
1.0	35.67	1.74	22.45	29.18	2.43	25.62	20.17	6.45	46.97	-27.4	3.32	-32.83
1.5	1.17	1.10	0.46	1.69	1.88	1.15	4.31	6.47	10.06	-12.31	3.27	-14.54
2.0	0.06	0.84	0.02	0.17	1.57	0.10	1.39	6.33	3.18	-6.94	3.26	-8.17
Contribution to $\mu\mu$ signal [83]												
$\lambda_{22}^L = 1$ (Scenario RK1A)												
1.0	40.89	71.88	265.27	58.68	72.66	769.52	70.40	62.77	1595.21	-233.00	42.73	-3594.15
1.5	1.39	64.44	8.10	3.91	71.35	50.30	15.20	64.33	352.97	-105.00	42.59	-1614.37
2.0	0.08	52.62	0.36	0.44	70.15	5.60	5.00	64.22	115.92	-58.80	43.08	-914.54
$\lambda_{22}^R = 1$ (Scenario RK1B)												
1.0	38.91	71.74	1007.69	58.29	72.36	1522.36	70.43	62.69	1593.99	-82.52	49.17	-1464.79
1.5	1.32	64.18	30.64	3.81	68.62	94.40	15.21	64.20	352.57	-37.33	49.09	-661.52
2.0	0.07	52.50	1.36	0.42	63.79	9.78	5.00	64.53	116.48	-21.0	48.62	-368.53
$\lambda_{32}^L = 1$ (Scenario RK1C)												
1.0	35.67	71.59	230.45	28.93	72.74	379.76	20.00	63.49	458.17	-75.30	39.10	-1062.87
1.5	1.17	64.46	6.78	1.72	72.33	22.44	4.29	64.58	100.49	-33.70	39.82	-484.39
2.0	0.06	52.47	0.29	0.17	71.77	2.22	1.41	64.90	33.04	-19.00	40.12	-275.17
$\lambda_{32}^R = 1$ (Scenario RK1D)												
1.0	35.67	71.75	923.90	29.04	72.37	758.73	20.05	63.73	461.36	-26.29	45.77	-434.43
1.5	1.17	64.60	27.19	1.69	69.28	42.27	4.29	64.43	99.74	-11.84	46.32	-197.94
2.0	0.06	52.00	1.14	0.17	65.35	3.95	1.41	65.37	33.25	-6.69	46.64	-112.60

$pp \rightarrow Z' \rightarrow \ell\ell$ events for validation and compared our cut efficiencies (ϵ) with the experimental efficiencies \times detector acceptance to ensure they agree with each other. In Table VI, we show the production cross sections, cut efficiencies, and number of events surviving the cuts for different signal contributions for the $R_{D^{(*)}}$ -motivated and $R_{K^{(*)}}$ -motivated one-coupling scenarios, respectively. We obtain these numbers by setting the concerned coupling to unity. There are a few points to note here. Pair production is, in general, insensitive to new physics couplings. However, a mild sensitivity arises due to the model-dependent t -channel lepton exchange diagram that contributes to the pair production [see Fig. 3(b)]. In Scenario RD1A where only λ_{23}^L is nonzero, the pair production cross section is 40.87 fb for $M_{U_1} = 1$ TeV, whereas in Scenario

RD1B, it is 35.67 fb. This is because the t -channel lepton exchange contribution is larger in Scenario RD1A. In this scenario, the second-generation quarks contribute in the initial states with PDFs bigger than the b -PDF contributing in Scenario RD1B. A similar minor difference can be seen between Scenario RK1A and Scenario RK1B. In Scenario RK1A, the process $cc \rightarrow U_1 U_1$ through a neutrino exchange is present, but it is absent in Scenario RK1B causing the minor difference. The single production cross sections are relatively larger in scenarios where the second-generation quarks appear in the initial states than those where only b -quarks can appear.

The cut efficiencies for different production modes for $R_{K^{(*)}}$ scenarios are generally much higher compared to $R_{D^{(*)}}$ scenarios. This is mainly because the selection

efficiency of the τ in the final state is much lower compared to the muons. For instance, in the $R_{K^{(*)}}$ scenarios, the efficiency for pair production processes ϵ^p can be as high as 71% for $M_{U_1} = 1$ TeV, whereas for $R_{D^{(*)}}$ scenarios, it is only $\sim 2\%$. The hadronic BR of τ is $\sim 64\%$, and the τ -tagging efficiency is about 60%. Combining just these two factors we get a factor of $0.64^2 \times 0.6^2 \sim 1/7$ reduction in the efficiency for the two τ_{had} 's in the pair production final state. Note that all of pair and single productions and t -channel U_1 exchange contribute positively towards the dilepton signal, whereas the signal-background interference contributes negatively as it is destructive in nature. The minus signs in σ^{nr2} and \mathcal{N}^{nr2} indicate the destructive nature of the interference.

Before presenting our results, we list the publicly available HEP packages used at various stages of our analysis.

- (i) *Lagrangian and model files*: The Lagrangian terms defined in the previous section are implemented in the FeynRules package [114] to obtain the UFO model files [115].
- (ii) *Event generation*: Using the UFO model files, we generate signal events using the MADGRAPH5 Monte-Carlo event generator [116] at the leading order (LO). The NNPDF2.3LO PDFs [117] are used with default dynamical scales.⁴ Higher-order QCD corrections for the vLQ are not considered in this analysis as they are not available in the literature.
- (iii) *Showering and hadronization*: This is performed by passing the parton-level events to PYTHIA6 [118]. We use the MLM matching scheme [119,120] (up to two additional jets) with virtuality-ordered PYTHIA showers to avoid double counting of the matrix-element partons with parton showers.
- (iv) *Detector simulation*: We use DELPHES3.4.2 [121] (with ATLAS and CMS cards) to perform the detector simulations. The jet-clusterings are done using the FastJet package [122]. We use the anti- k_T algorithm [123] with the radius parameter $R = 0.4$.

V. EXCLUSION LIMITS

There are three free couplings λ_{23}^L , λ_{33}^L , and λ_{33}^R that take part in the $R_{D^{(*)}}$ scenarios. We show the current exclusion limits on these couplings taken one at a time in Fig. 5(a) from the latest LHC $\tau\tau$ resonance search data [82]. Similarly, the $R_{K^{(*)}}$ scenarios have four free couplings in total: λ_{22}^L , λ_{32}^L , λ_{22}^R , and λ_{32}^R . We use the latest CMS $\mu\mu$ resonance search data [83] to obtain exclusion limits on

these couplings by considering one of them at a time as shown in Fig. 5(b). These are the 95% (2σ) confidence level (CL) exclusion limits. To obtain the limits, we set all other couplings except the one under consideration to zero. The method we follow is the same as the one used in Ref. [81] and is elaborated on in Appendix B. From the left plot, we see that the limit on λ_{23}^L is more severe than on $\lambda_{33}^{L/R}$. This is because, for nonzero λ_{23}^L , there is a s -quark-initiated contribution to the t -channel U_1 exchange that interferes with the SM $ss \rightarrow \gamma^*/Z^* \rightarrow \tau\tau$ process. In the case of nonzero $\lambda_{33}^{L/R}$, the process is b -quark-initiated and, therefore, is suppressed by the small b -PDF. Among the offshell photon and Z -boson contributions to the signal-background (SB) interference, the second one dominates. Similarly, one can also understand the relatively weaker limits on $\lambda_{32}^{L/R}$ in Fig. 5(b).

Among the four sources of dilepton events [the pair and single production, t -channel U_1 exchange, and the SB interference], different processes play the dominating roles in deciding the limits in different mass ranges. We observe an interesting role switch in these plots. In the high mass region where the limits on λ reach high values ($\gtrsim 1$), the resonant productions are relatively less important (also see Fig. 4), and the nonresonant productions play the determining roles. However, for $M_{U_1} \lesssim 1.5$ TeV, mainly the resonant productions determine the limits, and all the λ -dependent contributions are small. This switch of roles can also be inferred from Fig. 6 where we show the same limits as in Fig. 5 but ignore the resonant contributions in the dilepton signal. Comparing Figs. 5 and 6 we see that for $M_{U_1} \lesssim 2.5$ TeV, the limits can vary significantly depending on whether one considers the resonant productions or not. Since the nonresonant processes do not depend on the U_1 branching ratios, for a low mass U_1 the limits thus obtained are strictly valid when the branching ratio of the decay $U_1 \rightarrow \tau j/\tau b$ mediated by the coupling λ is small. However, the limits in Fig. 5 are obtained assuming only one coupling is nonzero, i.e., maximum branching ratio for the $U_1 \rightarrow \tau j/\tau b$ decay mediated by the coupling λ . For a very heavy U_1 ($\gtrsim 3$ TeV) the resonant productions become negligible, and hence, the limits of Figs. 5 and 6 converge. We also observe that in the low mass region ($M_{U_1} \sim 1$ TeV) where the limit is determined almost solely by the pair production, the data are badly fitted by the U_1 events (i.e., $\chi_{\min}^2/\text{d.o.f.} \gg 1$). This suggests that the dimuon data disfavor pair production of a ~ 1 TeV U_1 —this is similar to but independent of the direct LQ search limits.

We plot the relevant direct search limits from the $jj + \cancel{E}_T$ and $tt + \cancel{E}_T$ channels [85] together with the limits on the $R_{D^{(*)}}$ scenarios with one coupling in Figs. 7(a) and 7(b). We also show the parameter regions that are favored by the $R_{D^{(*)}}$ observables and consistent with the relevant flavor

⁴The NNPDF2.3LO PDF for the heavy quarks might have considerable uncertainties. However, our results, i.e., the limits on the U_1 parameters, are largely insensitive to these.

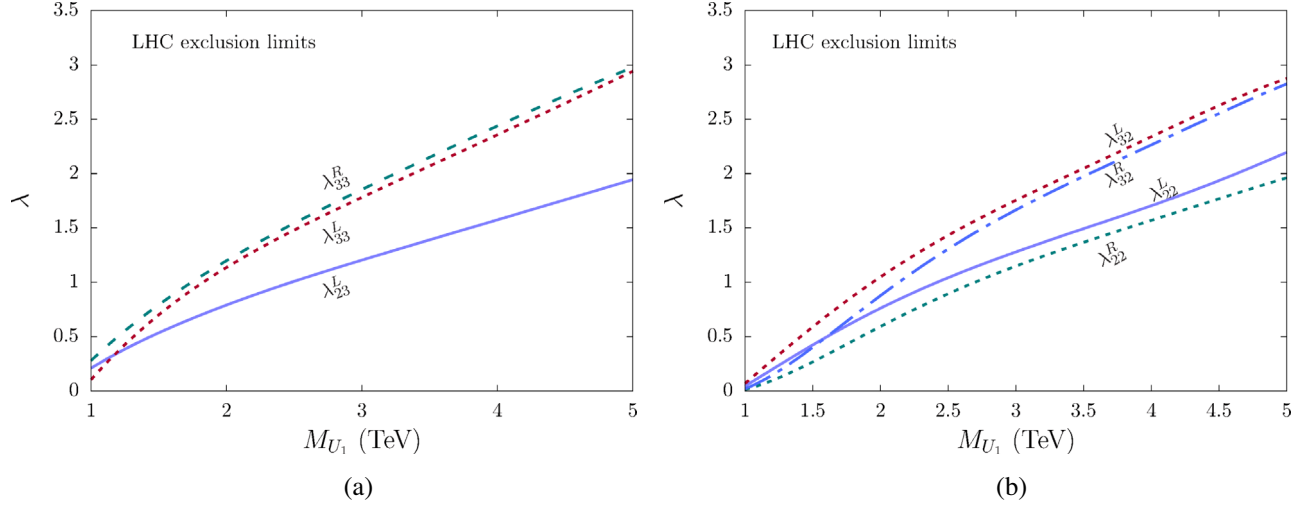


FIG. 5. The 2σ LHC exclusion limits on the couplings participating in the (a) $R_{D^{(*)}}$ and (b) $R_{K^{(*)}}$ scenarios. The regions above these lines are excluded. These exclusion limits are obtained by recasting the dilepton search data [82,83] with a combination of all possible U_1 production processes that can contribute to the dilepton final states.

observables (as discussed in Section II) in the same plots. We see that in Scenario RD1A, the region marked as FlavD, which is defined as

$$\text{FlavD} \equiv \text{the region allowed by } \{R_{D^{(*)}} + F_L(D^*) + P_\tau(D^*) + \mathcal{B}(B_{(c)} \rightarrow \tau\nu) + \mathcal{C}_9^{\text{univ}}\} \quad (67)$$

is in tension with the $B_s - \bar{B}_s$ mixing data and is independently and entirely excluded by the $\tau\tau$ data. The tension between FlavD and the $B_s - \bar{B}_s$ mixing data arises since the $B_s - \bar{B}_s$ mixing data favors a smaller $\mathcal{C}_{V_L}^{U_1}$

(via $\mathcal{C}_{\text{box}}^{U_1}$ which roughly goes as the square of $\mathcal{C}_{V_L}^{U_1}$) than the $R_{D^{(*)}}$ observables. Scenario RD1B does not contribute to Eq. (17) and hence cannot accommodate a nonzero $\mathcal{C}_9^{\text{univ}}$. We mark the parameter region favored by the $R_{D^{(*)}}$ observables in this scenario as FlavD₉ which stands for the region allowed by all the constraints included in FlavD except $\mathcal{C}_9^{\text{univ}}$, i.e.,

$$\text{FlavD}_9 \equiv \text{the region allowed by } \{R_{D^{(*)}} + F_L(D^*) + P_\tau(D^*) + \mathcal{B}(B_{(c)} \rightarrow \tau\nu)\}. \quad (68)$$

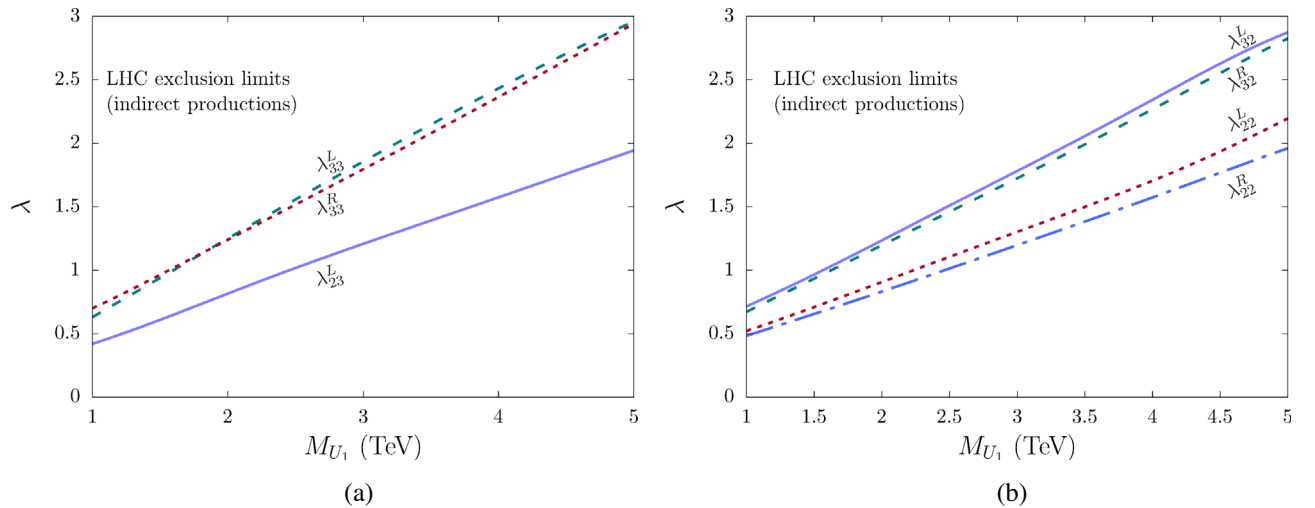


FIG. 6. These exclusion plots are similar to the ones in Fig. 5, but they are obtained only for the nonresonant production and its interference with the SM background. Comparing with Fig. 5, they show that in the lower mass region, the contribution of the resonant U_1 productions is significant. However, in the higher mass region, the nonresonant production and its interference with the SM background determine the limits.

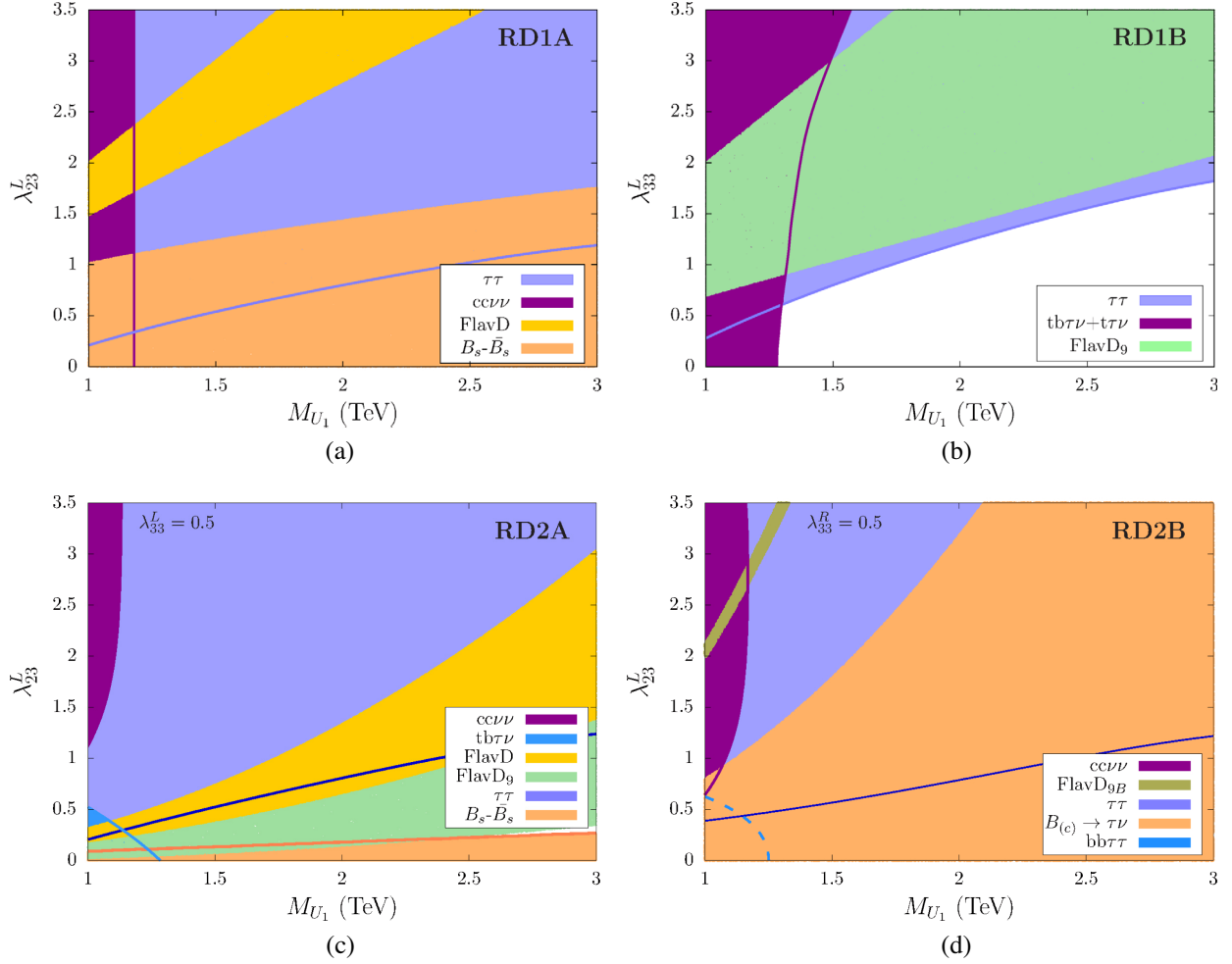


FIG. 7. The 2σ exclusion limits from the LHC and the preferred regions by the flavor anomalies. The purple regions are excluded at 2σ by the ATLAS $\tau\tau$ data [82]. The magenta and blue regions depict the excluded mass ranges from direct searches. (a) Scenario RD1A: Only λ_{23}^L is nonzero. The FlavD region (yellow), defined in Eq. (67), is favored by the $R_{D^{(*)}}$ anomalies. The light orange region is favored by $B_s - \bar{B}_s$ mixing. The direct detection mass limit (magenta) is from the CMS search in the $cc\nu\nu$ channel [85]. (b) Scenario RD1B: Only λ_{33}^L is nonzero. The FlavD₉ region (green) agrees with all the constraints in FlavD except $\mathcal{C}_9^{\text{univ}}$ [Eq. (18)] since the corresponding operator, $\mathcal{O}_9^{\text{univ}}$, cannot be generated in this scenario. The magenta region here depicts the limits from the very recent CMS combined search in the $t b \tau \nu + \tau \nu$ channel [88]. We have recast the observed events data to extrapolate the limit for $\lambda_{33}^L > 2.5$. There is no $B_s - \bar{B}_s$ mixing in this scenario. (c) Scenario RD2A: $\lambda_{33}^L = 0.5$ (benchmark choice), and λ_{23}^L is free. The magenta and blue regions are the limits from the direct searches at CMS [85,88]. (d) Scenario RD2B: $\lambda_{33}^R = 0.5$ (benchmark choice), and λ_{23}^L is free. The blue dashed line shows the limits from the ATLAS $b b \tau \tau$ direct search data [87]. The dashed line implies that the recast has been done from a scalar LQ direct search. The FlavD_{9B} region (olive green), defined in Eq. (69), agrees with all the constraints in the FlavD₉ region without the constraints from the $B_{(c)} \rightarrow \tau\nu$ decays. The light orange color shows the region preferred by $B_{(c)} \rightarrow \tau\nu$.

From Fig. 7(b), we see that for this strictly one-coupling scenario, the entire FlavD₉ is excluded by the latest $\tau\tau$ data.

If we look at the two-coupling scenarios, the situation somewhat improves. For example, in Figs. 7(c) and 7(d), we show a projection of the three-dimensional parameter space of Scenario RD2A and Scenario RD2B, respectively. In Fig. 7(c), we keep $\lambda_{33}^L = 0.5$ and let λ_{23}^L and M_{U_1} vary (Scenario RD2A). We see that a good part of the FlavD₉ region (note that the FlavD is a subregion within FlavD₉)

survives the LHC bounds, but a large part of it remains in conflict with the $B_s - \bar{B}_s$ mixing data. However, a small part of FlavD₉ does agree with $B_s - \bar{B}_s$ mixing and survives the LHC bounds. We show two more projections of the parameter space of Scenario RD2A in Figs. 8(a) and 8(c)—we let λ_{23}^L and λ_{33}^L vary and keep the mass of U_1 fixed. There we show the region allowed by the LHC data and the relevant flavor regions for $M_{U_1} = 1.5(2.0)$ TeV, respectively. In absence of λ_{33}^L , Scenario RD2B cannot accommodate the allowed $\mathcal{C}_9^{\text{univ}}$, and, in this case, the

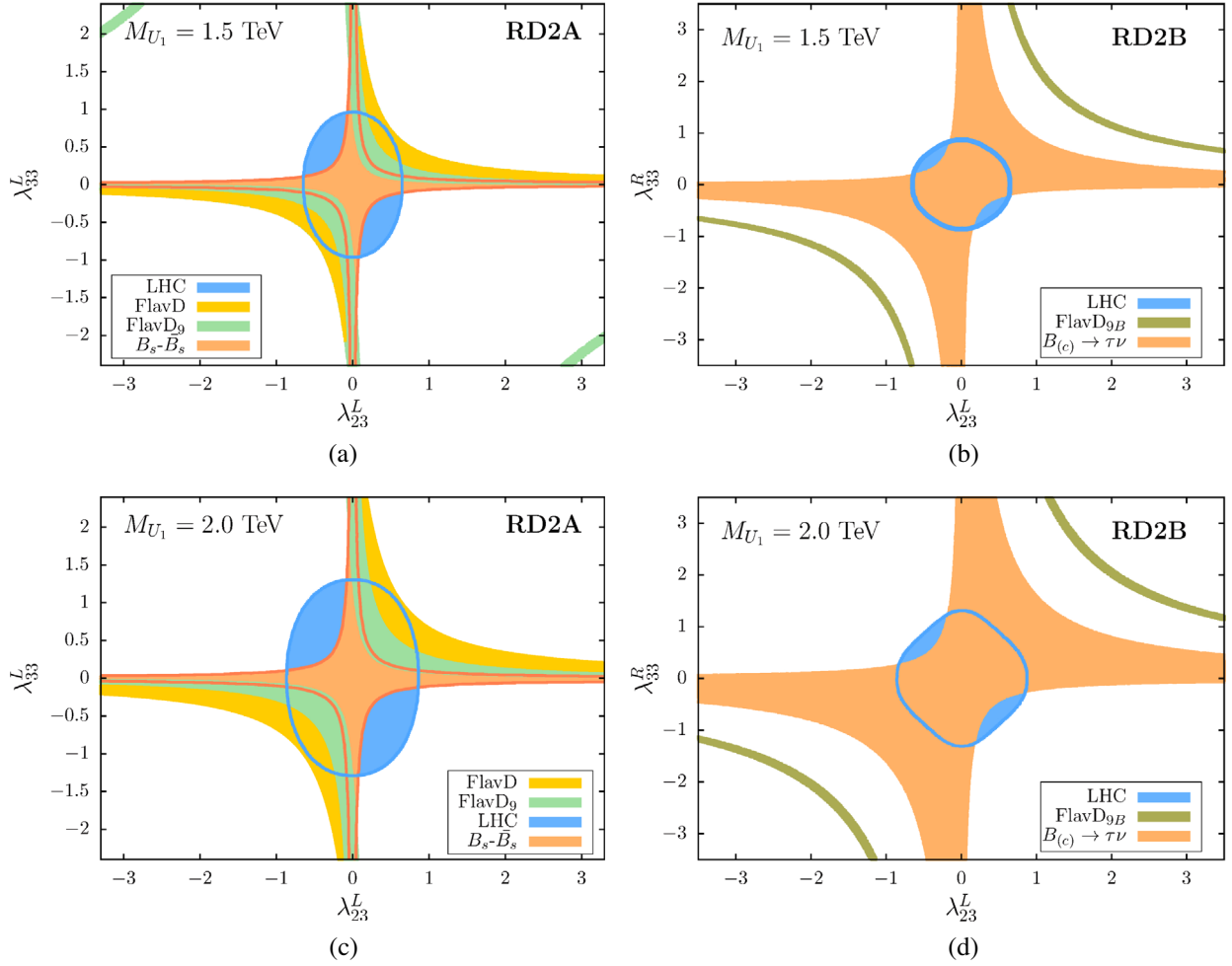


FIG. 8. The regions favored by the flavor observables (yellow, green, and orange) and allowed by the LHC data (blue). We consider two benchmark mass values, $M_{U_1} = 1.5$ TeV and 2 TeV. (a) and (c) Scenario RD2A ($\lambda_{33}^R = 0$): FlavD (yellow) and FlavD₉ (green) are the regions preferred by the flavor anomalies with and without the $\mathcal{O}_9^{\text{univ}}$ operator, respectively. The light orange region is favored by the $B_s - \bar{B}_s$ mixing. (b) and (d) Scenario RD2B ($\lambda_{33}^R = 0$): The light orange color marks the regions preferred by the $B_{(c)} \rightarrow \tau\nu$ decay. FlavD_{9B} (olive green) shows the region preferred by the flavor anomalies except $\mathcal{O}_9^{\text{univ}}$ and the $B_{(c)} \rightarrow \tau\nu$ decay.

region favored by the $R_{D^{(*)}}$ observable stands in conflict with the $\mathcal{B}(B_{(c)} \rightarrow \tau\nu)$ constraint—see the region marked as FlavD_{9B} for the region allowed by all the constraints included in FlavD₉ except $\mathcal{B}(B_{(c)} \rightarrow \tau\nu)$, i.e.,

$$\text{FlavD}_{9B} \equiv \text{the region allowed by } \{R_{D^{(*)}} + F_L(D^*) + P_\tau(D^*)\}. \quad (69)$$

$$\text{FlavK} \equiv \text{the region favored by } \{\text{the global fits to } b \rightarrow s\mu\mu \text{ data} + B_s - \bar{B}_s \text{ mixing}\} \quad (70)$$

in the one-coupling scenarios [except for Scenario RD2B where, as already pointed out, λ_{32}^L alone cannot explain the $R_{K^{(*)}}$ anomalies. Hence, in Fig. 9(b) we only show the

From Fig. 7(d) [where we keep $\lambda_{33}^R = 0.5$ and let λ_{23}^L and M_{U_1} vary (Scenario RD2B)], we see that the entire FlavD_{9B} region is ruled out by the LHC data. This can also be seen from the two coupling plots in Figs. 8(b) and 8(d).

In Fig. 9, we compare the bounds on λ_{22}^L , λ_{32}^L , λ_{22}^R , and λ_{32}^R from the CMS $\mu\mu$ data [83] with the regions favored by the $R_{K^{(*)}}$ anomalies and allowed by the $B_s - \bar{B}_s$ mixing data marked as

region allowed by the $B_s - \bar{B}_s$ mixing data]. In these plots, we also show the recast limits from the recent pair production search by the ATLAS Collaboration that

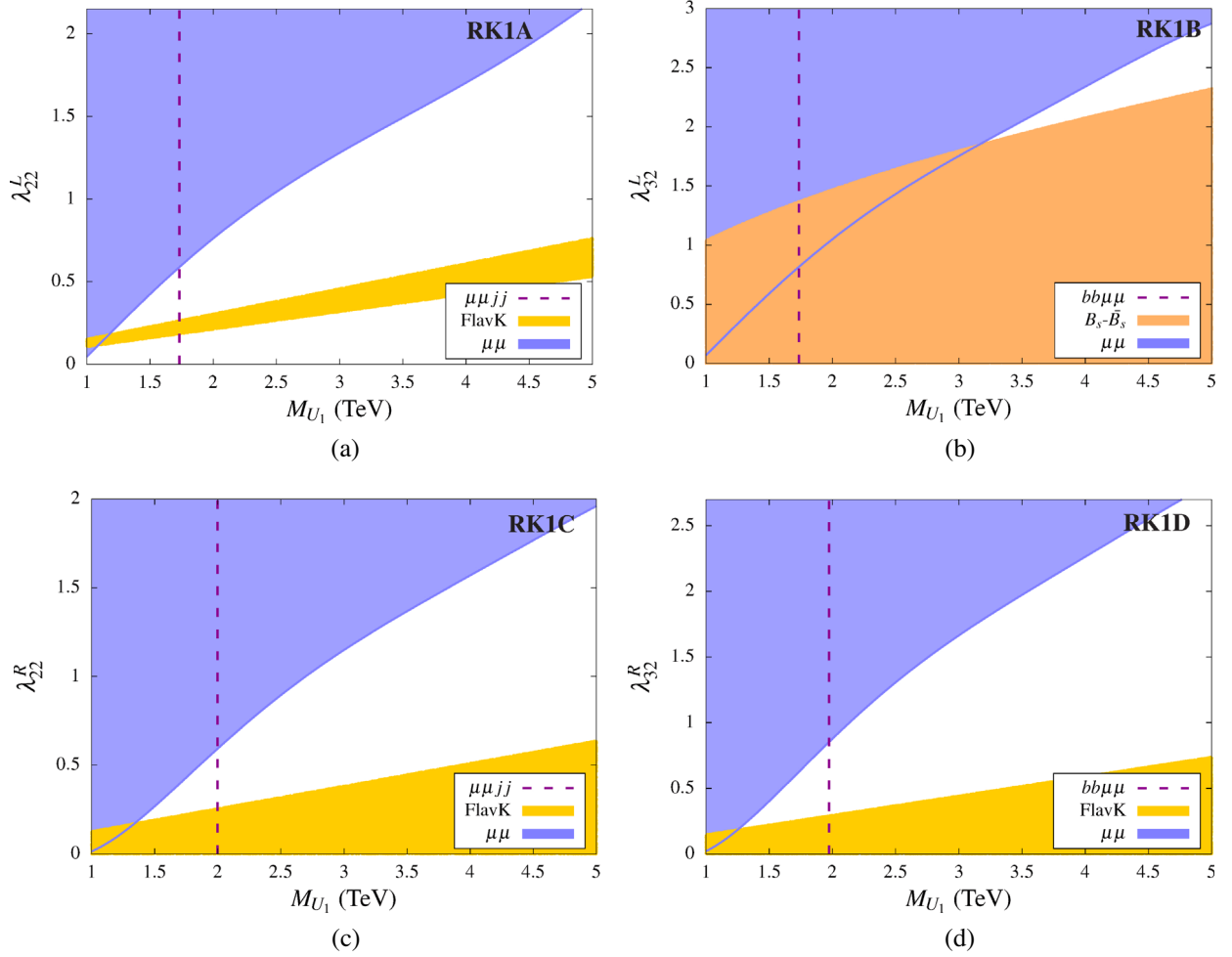


FIG. 9. The regions excluded at 2σ by the CMS $\mu\mu$ search data [83] in the minimal $R_{K^{(*)}}$ scenarios (violet). FlavK (yellow), defined in Eq. (70), is the region favored by the global fits to the $b \rightarrow s\mu\mu$ and $B_s - \bar{B}_s$ mixing. (a) Scenario RK1A: Only λ_{22}^L is nonzero. (b) Scenario RK1B: Only λ_{32}^L is nonzero. Since, λ_{32}^L alone cannot explain the $R_{K^{(*)}}$ anomalies, we only show the region allowed by the $B_s - \bar{B}_s$ mixing data. (c) Scenario RK1C: Only λ_{22}^R is nonzero. (d) Scenario RK1D: Only λ_{32}^R is nonzero. The magenta dashed lines denote the recast exclusion limits from the ATLAS direct search for pair production of scalar LQs in the $\mu\mu + jj/bb$ channels [86].

effectively rule out U_1 masses almost up to 2 TeV. To obtain these limits we have recast the recent ATLAS search for scalar LQ in the $\mu\mu + jj/bb$ channel obtained with 139 fb^{-1} of integrated luminosity [86].⁵ We see the LHC $\mu\mu$ data are much less restrictive on the FlavK regions than the $\tau\tau$ data on the FlavD regions. This is mainly because the magnitudes of these couplings required to explain the $R_{K^{(*)}}$ anomalies are much smaller than those in the $R_{D^{(*)}}$ scenarios. We also note that the direct search mass exclusion limits are weaker in the scenarios with left-type couplings (i.e., Scenario RK1A and Scenario RK1B) than those with right-type couplings (Scenario RK1C and

Scenario RK1D). This is because the decay $U_1 \rightarrow \mu b/\mu j$ has 100% BR in the right-type coupling scenarios instead of the 50% in the left-type ones. The recast limits imply that a 1.5 TeV U_1 is ruled out in all the two-coupling scenarios. Hence we consider a 2 TeV U_1 in the two-coupling scenarios in Fig. 10. There we show the regions allowed by the LHC data along with the FlavK regions in Scenario RK2A and Scenario RK2D and FlavK_B regions in Scenario RK2B and Scenario RK2C. In the last two scenarios, the constraints from $B_s - \bar{B}_s$ mixing data are not applicable, and the FlavK_B regions are just the ones favored by the global fit of $b \rightarrow s\mu\mu$ data

⁵We show the recast ATLAS limits [86] only with dashed lines because, strictly speaking, the search was optimized for a scalar LQ. In our recast for U_1 , we have assumed that the selection efficiencies remain unchanged when one switches from the pair production of scalar LQs to that of the vector ones.

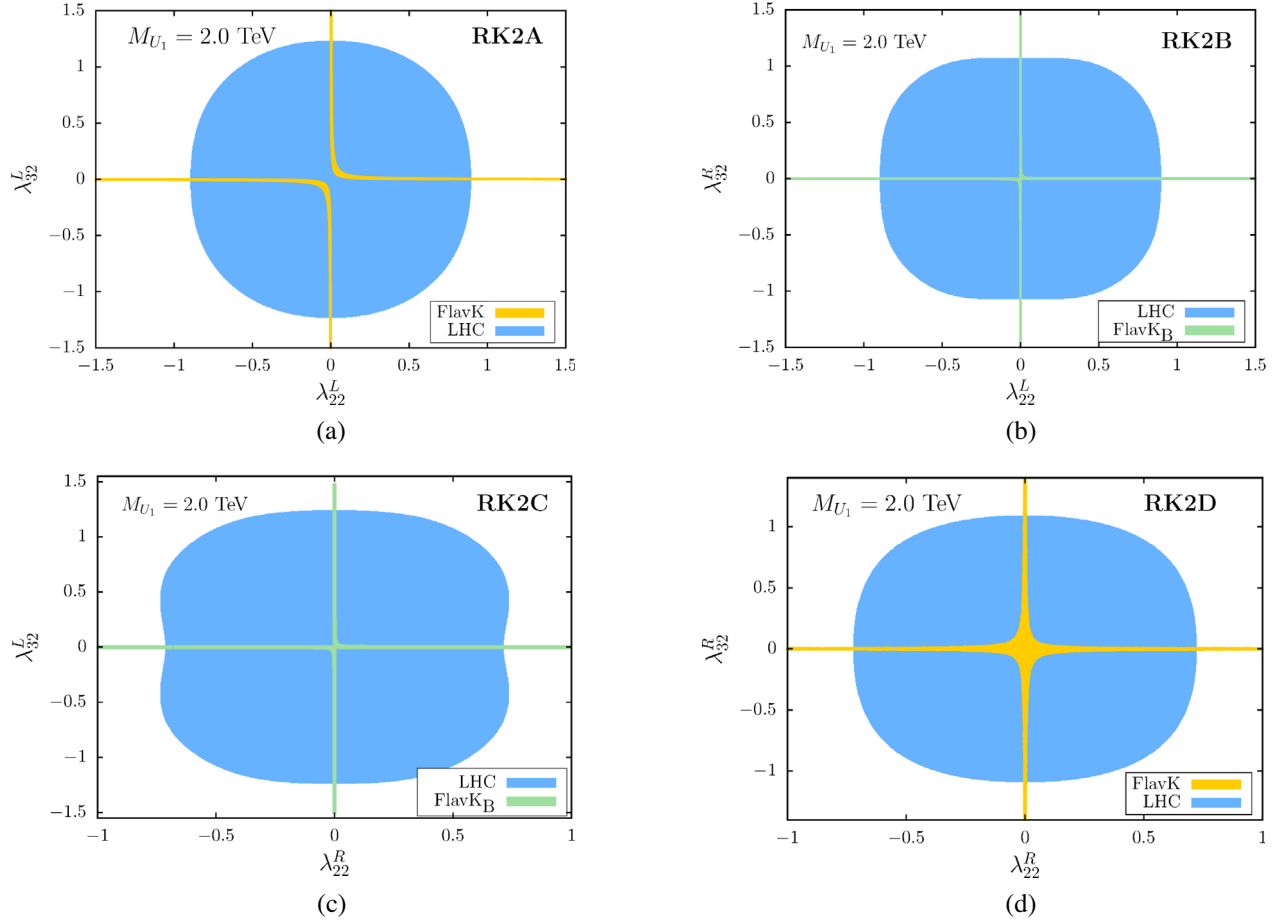


FIG. 10. The regions favored by the $R_{K^{(*)}}$ observables (yellow and green) and allowed by the LHC data (blue). The blue regions are obtained by recasting the CMS $\mu\mu$ search data [83]. (a) and (d) In Scenario RK2A and Scenario RK2D, the FlavK region (yellow) depicts the allowed regions by the $b \rightarrow s\mu\bar{\mu}$ global fits and $B_s - \bar{B}_s$ mixing. (b) and (c) In Scenario RK2B and Scenario RK2D, there is no restriction from the $B_s - \bar{B}_s$ mixing. FlavK_B (green), defined in Eq. (71), stands for the region preferred by the $b \rightarrow s\mu\bar{\mu}$ global fits alone.

$$\begin{aligned} \text{FlavK}_B &\equiv \text{FlavK} + \text{the region exclusively disfavored by } B_s - \bar{B}_s \text{ mixing} \\ &\equiv \text{the region favored by the global fits to } b \rightarrow s\mu\bar{\mu} \text{ data.} \end{aligned} \quad (71)$$

The recast ATLAS scalar search limits however does not entirely rule out a 1.5 TeV U_1 solution for the $R_{K^{(*)}}$ anomalies. To see this, one needs to make $\beta(U_1 \rightarrow \mu b/\mu j) \lesssim 0.25$ by introducing additional nonzero coupling(s). For example, in Fig. 11 we show that for $\lambda_{23}^L = 0.006$ and $\lambda_{33}^L = 0.93$ [a point we chose randomly from the FlavD₉ region in Fig. 8(a) that agrees with $B_s - \bar{B}_s$

mixing and is allowed by the LHC data] all the two-coupling $R_{K^{(*)}}$ scenarios survive the recast bounds for $M_{U_1} = 1.5$ TeV. This is interesting, as it explicitly shows four possible parameter choices for which a 1.5 TeV U_1 can account for both the $R_{D^{(*)}}$ and $R_{K^{(*)}}$ anomalies. These choices are, of course, only illustrative, not unique or special.

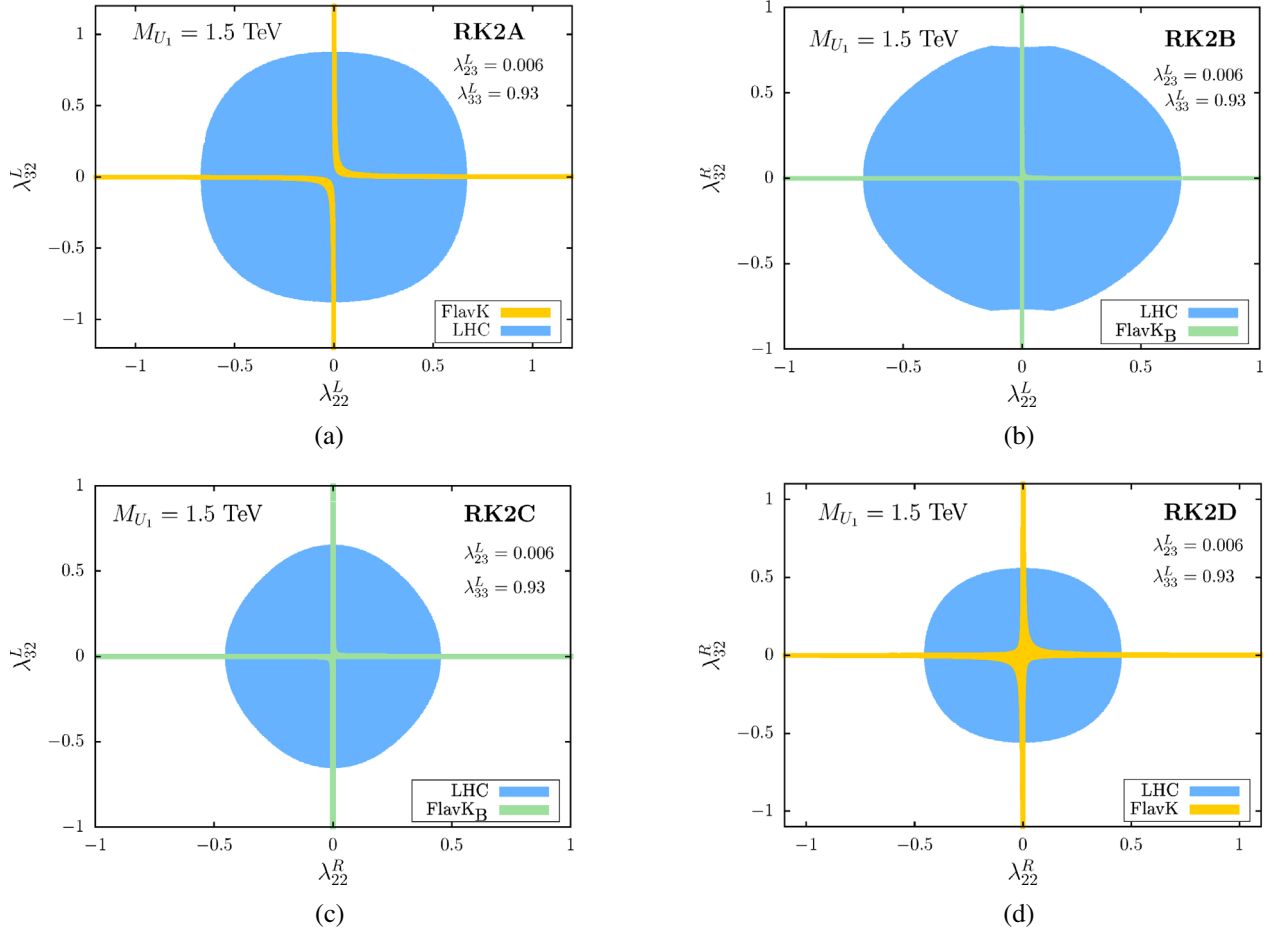


FIG. 11. Examples of regions in the parameter space of a 1.5 TeV U_1 surviving the LHC limits and simultaneously accommodating the $R_{D^{(*)}}$ and $R_{K^{(*)}}$ anomalies. The FlavK (yellow), FlavK_B (green), and the blue regions are identical to the ones in Fig. 10. When we recast the ATLAS search in the $\mu\mu + bb/jj$ channels [86], the presence of the additional couplings, $\lambda_{23}^L = 0.006$ and $\lambda_{33}^L = 0.93$ [allowed by the LHC and flavor data, see Fig. 8(a)], relaxes the exclusion limits, thus allowing the otherwise excluded mass value in the $R_{K^{(*)}}$ two-coupling scenarios.

VI. SUMMARY AND CONCLUSIONS

In this paper, we have derived precise limits on a flavor-anomalies-motivated U_1 LQ model using the latest LHC and flavor data. We started with a generic coupling texture for U_1 (with seven free couplings) that can contribute to the $R_{D^{(*)}}$ and $R_{K^{(*)}}$ observables. Taking a bottom-up approach, suitable for obtaining bounds from the existing LHC searches, we constructed all possible one- and two-coupling scenarios that can accommodate either the $R_{D^{(*)}}$ or $R_{K^{(*)}}$ anomalies. In particular, we considered two one-coupling and two two-coupling scenarios that can give rise to the $b\tau U_1$ and $c\nu U_1$ couplings required by the $R_{D^{(*)}}$ observables. Similarly, we considered four one-coupling and four two-coupling scenarios contributing to the $b \rightarrow s\mu^+\mu^-$ transition. We recast the current LHC dilepton searches ($\tau\tau$ and $\mu\mu$) [82,83] to obtain limits on the U_1 couplings for a range of M_{U_1} in these scenarios. We also looked at the bounds from the latest direct LQ searches from ATLAS and CMS. Whenever needed, we recast the

latest scalar LQ searches in terms of U_1 parameters as these were found to give better limits than the existing ones. Put together, our results give the best limits on the U_1 parameters currently available from the LHC. These bounds are independent of and complementary to other flavor bounds.

Previously, the high- p_T dilepton data were used to put limits on the U_1 couplings. Most of these analyses, however, focused only on the nonresonant t -channel U_1 exchange process. However, we found that this process interferes destructively with the SM background, and, in most cases, it is this interference that plays the prominent role in setting the exclusion limits, especially for a heavy U_1 . Also, other resonant production processes, namely, the pair and the single productions of U_1 , can also contribute significantly to the high- p_T dilepton tails. We have shown the differences that the inclusion of resonant production processes can make on the exclusion limits in Figs. 5 and 6. The limits we obtained are robust as they depend only on a few assumptions about the underlying model. They are also

precise as all the resonant and nonresonant contributions including the signal-background interference are systematically incorporated in our statistical recast of the dilepton data. The low mass regions are bounded by the direct pair production search limits that depend only on the BRs. When U_1 is heavy, the limits mostly come from the nonresonant process and its interference with the SM background that depend only on the value of the coupling(s) involved, not on the BRs.

We found that in the minimal (with one free coupling) or some of the next-to-minimal (with two free couplings) scenarios, the parameter spaces required to accommodate the $R_{D^{(*)}}$ anomalies are already ruled out or in tension with the latest LHC data (see e.g. Figs. 7 and 8). In some scenarios, the regions favored by the anomalies are in conflict with other flavor bounds, but in the RD1B minimal scenario, a part of the parameter space survives the LHC bounds [see Fig. 7(b)] that can explain the $R_{D^{(*)}}$ anomalies. We found that a good part of the parameter space required to explain the $R_{K^{(*)}}$ anomalies survives the dilepton bounds, except the recent ATLAS search for scalar LQ in the $\mu\mu + jj/bb$ channel [86] put some pressure for $M_{U_1} \lesssim 2$ TeV (see Figs. 9 and 10).

Our method for obtaining bounds is generic. It is possible to extend our analysis to scenarios with more nonzero couplings and/or additional degrees of freedom by considering our scenarios as templates. As an example, we showed the bounds on a combined scenario with three free couplings ($\lambda_{33}^L, \lambda_{32}^{L/R}, \lambda_{22}^{L/R}$) that can accommodate both the $R_{D^{(*)}}$ and $R_{K^{(*)}}$ anomalies simultaneously with a 1.5 TeV U_1 in Fig. 11 (even though a simple recast of the recent ATLAS LQ search in the $\mu\mu + jj/bb$ channel rules out a U_1 of mass 1.5 TeV that decays to these final states exclusively [86]). One should therefore keep in mind that a U_1 LQ with mass $\lesssim 2$ TeV is still allowed and can resolve the B -anomalies). To obtain limits on other general scenarios, one can use the parametrization and method elaborated in Appendixes A and B.

We also identified some possible new search channels of U_1 that have not been considered so far. Our simple parametrization of various possible scenarios in terms of a few parameters can serve as a guide for the future U_1 searches at the LHC. It can also be used for interpreting the results of future bottom-up experimental searches of vLQs.

ACKNOWLEDGMENTS

A. B. and S. M. acknowledge support from the Science and Engineering Research Board (SERB), DST, India, under Grant No. ECR/2017/000517. D. D. acknowledges the DST, Government of India for the INSPIRE Faculty Fellowship (Grant No. IFA16-PH170). T. M. is supported by the intramural grant from Indian Institute of Science Education and Research, Thiruvananthapuram. C. N. is supported by the DST-Inspire Fellowship.

APPENDIX A: CROSS SECTION PARAMETRIZATION FOR THE $\ell\ell$ SIGNAL PROCESSES

It is not straightforward to obtain precise LHC exclusion limits from the dilepton data when multiple couplings are nonzero simultaneously. This is mainly because different couplings contribute to different topologies with the same final states. In multi-coupling scenarios, the presence of substantial signal-background interference and/or signal-signal interference complicates the picture further. All these possibilities are present in the U_1 scenarios considered here. Therefore, a discussion on a systematic approach to properly take care of these complications might be useful for the reader. Below, we discuss the method we have used for multi-coupling scenarios in the context of U_1 . However, this method is not limited to U_1 and $\tau\tau$ or $\mu\mu$ final states but can be adapted easily for any BSM scenarios wherever needed.

1. Pair production

As mentioned in Section III, the pair production of U_1 is not fully model-independent. It depends on two parameters— κ , parametrizing the new kinetic terms, and λ , the generic coupling for $\ell q U_1$ interactions. In our analysis, we have set $\kappa = 0$. The dependence on λ enters in the pair production through the t -channel lepton exchange diagrams. If n different new couplings (λ_i with $i = \{1, 2, 3, \dots, n\}$) are contributing, the total cross section for the process $pp \rightarrow U_1 U_1$ can be expressed as

$$\begin{aligned} \sigma^p(M_{U_1}, \lambda) &= \sigma^{p_0}(M_{U_1}) + \sum_i^n \lambda_i^2 \sigma_i^{p_2}(M_{U_1}) \\ &+ \sum_{i \geq j}^n \lambda_i^2 \lambda_j^2 \sigma_{ij}^{p_4}(M_{U_1}), \end{aligned} \quad (\text{A1})$$

where the sums go up to n . The σ^{p_x} functions on the rhs depend only on the mass of U_1 . Here, $\sigma^{p_0}(M_{U_1})$ is the λ -independent part determined by the strong coupling constant. This part can be computed taking $\lambda_i \rightarrow 0$ for all the new couplings. The $\sigma_i^{p_2}(M_{U_1})$ terms originate from the interference between the QCD-mediated model-independent diagrams and the t -channel lepton exchange diagrams. The $\sigma_{ij}^{p_4}(M_{U_1})$ terms are from the pure t -channel lepton exchange diagrams.

For a particular M_{U_1} , there are n unknown $\sigma_i^{p_2}$ and $n(n+1)/2$ unknown $\sigma_{ij}^{p_4}$ functions that we need to find out. For that, we compute σ^p for $n(n+3)/2$ different values of λ_i and solve the resulting linear equations. We repeat the same procedure for different mass points. We can now get $\sigma^p(M_{U_1}, \lambda)$ for any intermediate value of M_{U_1} either from numerical fits to direct evaluation.

In the presence of kinematic selection cuts, different $\sigma^{p_x}(M_{U_1})$ parts contribute differently to the surviving

events. Hence, the overall cut efficiency for the pair production process e^p depends on both M_{U_1} and λ . The total number of surviving events from the pair production process passing through some selection cuts can, therefore, be expressed as

$$\begin{aligned} \mathcal{N}^p &= \sigma^p \circ e^p(M_{U_1}, \lambda) \times \mathcal{B}^2(M_{U_1}, \lambda) \times L \\ &= \left\{ \sigma^{p_0} \times e^{p_0} + \sum_i^n \lambda_i^2 \sigma_i^{p_2} \times e_i^{p_2} \right. \\ &\quad \left. + \sum_{i \geq j}^n \lambda_i^2 \lambda_j^2 \sigma_{ij}^{p_4} \times e_{ij}^{p_4} \right\} \times \mathcal{B}^2(M_{U_1}, \lambda) \times L, \quad (\text{A2}) \end{aligned}$$

where all e^{p_x} depend only on M_{U_1} . Here L is the integrated luminosity, and $\mathcal{B}(M_{U_1}, \lambda)$ is the relevant branching ratio (of the decay mode of U_1 that contributes to the signal) which can be obtained analytically. The $e^{p_x}(M)$ functions can be obtained by computing the fraction of events surviving the selection cuts while computing the $\sigma^{p_x}(M_{U_1})$ functions.

2. Single production

As discussed earlier, single production of U_1 usually contains two types of contributions $U_1 x$ and $U_1 yz$ (where x, y, z are SM particles). The amplitudes of the $U_1 x$ type of processes are always proportional to λ . But $U_1 yz$ amplitudes can have both linear and cubic terms in λ . Therefore, the most generic form of the single production process $pp \rightarrow U_1 x + U_1 yz$ can be expressed as

$$\sigma^s(M, \lambda_i) = \sum_i^n \lambda_i^2 \sigma_i^{s_2}(M_{U_1}) + \sum_{i \geq j \geq k}^n \lambda_i^2 \lambda_j^2 \lambda_k^2 \sigma_{ijk}^{s_6}(M_{U_1}). \quad (\text{A3})$$

The $\sigma^{s_x}(M)$ functions can be obtained following the same method used for pair production. We can express the total number of single production events as

$$\begin{aligned} \mathcal{N}^s &= \sigma^s \circ e^s(M_{U_1}, \lambda) \times \mathcal{B}(M_{U_1}, \lambda) \times L \\ &= \left\{ \sum_i \lambda_i^2 \sigma_i^{s_2}(M_{U_1}) \times \epsilon_i^{s_2}(M_{U_1}) \right. \\ &\quad \left. + \sum_{i \geq j \geq k} \lambda_i^2 \lambda_j^2 \lambda_k^2 \sigma_{ijk}^{s_6}(M_{U_1}) \times \epsilon_{ijk}^{s_6}(M_{U_1}) \right\} \\ &\quad \times \mathcal{B}(M_{U_1}, \lambda_i) \times L. \quad (\text{A4}) \end{aligned}$$

3. Nonresonant production

The t -channel U_1 exchange processes fall in this category. There are two different sources of nonresonant contributions one has to consider. One is from the signal-SM background interference and is proportional to λ_i^2 .

The other is from the signal-signal interference and hence is quartic in λ . We can express the total nonresonant $pp \rightarrow xy$ cross section as

$$\sigma^{nr}(M_{U_1}, \lambda) = \sum_i^n \lambda_i^2 \sigma_i^{nr_2}(M_{U_1}) + \sum_{i \geq j}^n \lambda_i^2 \lambda_j^2 \sigma_{ij}^{nr_4}(M_{U_1}). \quad (\text{A5})$$

Note that $\sigma^{nr}(M_{U_1}, \lambda)$ can be negative when the signal-background interference is destructive. Indeed, this is the case we observe for U_1 . By introducing the $\epsilon(M_{U_1})$ functions, the total number of surviving events can be written as

$$\begin{aligned} \mathcal{N}^{nr} &= \sigma^{nr} \circ e^{nr}(M_{U_1}, \lambda) \times L \\ &= \left\{ \sum_i^n \lambda_i^2 \sigma_i^{nr_2}(M_{U_1}) \times \epsilon_i^{nr_2}(M_{U_1}) \right. \\ &\quad \left. + \sum_{i \geq j}^n \lambda_i^2 \lambda_j^2 \sigma_{ij}^{nr_4}(M_{U_1}) \times \epsilon_{ij}^{nr_4}(M_{U_1}) \right\} \times L. \quad (\text{A6}) \end{aligned}$$

Notice, no BR appears in the above equation. A negative $\sigma^{nr}(M_{U_1}, \lambda)$ makes \mathcal{N}^{nr} a negative number as presented in Table VI.

For an illustration, we show the observed $\mu\mu$ data [83] and the corresponding SM contributions in Fig. 12. In the lower panel we show the different signal components for $M_{U_1} = 1.5$ TeV and $\lambda_{22}^L = 1$ (Scenario RK1A).

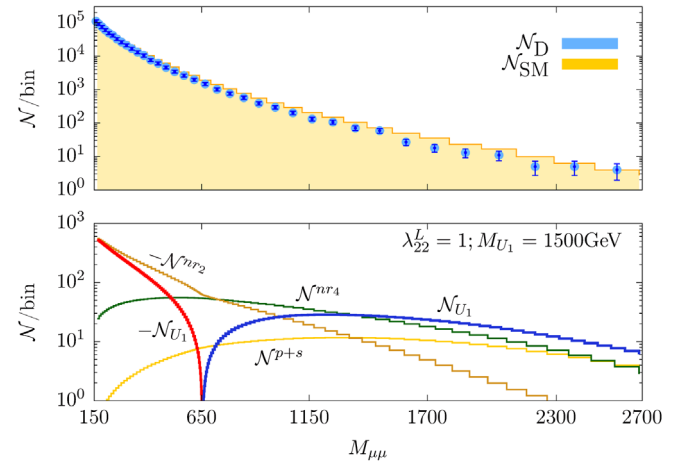


FIG. 12. The observed $M_{\mu\mu}$ distribution and the corresponding SM contributions from Ref. [83]. The errors are obtained using Eq. (B3). (Lower panel) The different signal components for a typical choice of parameters, $M_{U_1} = 1.5$ TeV and $\lambda_{22}^L = 1$ (Scenario RK1A). The number of U_1 signal events are denoted by \mathcal{N}_{U_1} [Eq. (B2)], and $\mathcal{N}^{p+s} = \mathcal{N}^p + \mathcal{N}^s$ denotes the events from pair and single production processes. Among the nonresonant contributions, \mathcal{N}^{nr_2} denotes the SM-BSM interference, and \mathcal{N}^{nr_4} is the pure BSM nonresonant part.

APPENDIX B: LIMITS ESTIMATION: χ^2 TESTS

To obtain the limits on the parameter space in various U_1 scenarios, we recast the LHC $\tau\tau$ and $\mu\mu$ search data [82,83]. In particular, we perform χ^2 tests to estimate the limits on parameters from the transverse (invariant) mass distribution of the $\tau\tau$ ($\mu\mu$) data. The method is essentially the same as the one used in Ref. [81] for S_1 LQ. Here we briefly outline the steps.

- (1) For each distribution, the test statistic can be defined as

$$\chi^2 = \sum_i \left(\frac{\mathcal{N}_T^i(M_{U_1}, \lambda) - \mathcal{N}_D^i}{\Delta\mathcal{N}^i} \right)^2, \quad (\text{B1})$$

where the sum runs over the corresponding bins. Here, $\mathcal{N}_T^i(M_{U_1}, \lambda)$ stands for expected (theory) events, and \mathcal{N}_D^i is the number of observed events in the i th bin. The number of theory events in the i th bin can be expressed

$$\begin{aligned} \mathcal{N}_T^i(M_{U_1}, \lambda) &= \mathcal{N}_{U_1}^i(M_{U_1}, \lambda) + \mathcal{N}_{\text{SM}}^i \\ &= [\mathcal{N}^p(M_{U_1}, \lambda) + \mathcal{N}^s(M_{U_1}, \lambda) \\ &\quad + \mathcal{N}^{nr}(M_{U_1}, \lambda)] + \mathcal{N}_{\text{SM}}^i. \end{aligned} \quad (\text{B2})$$

Here, $\mathcal{N}_{U_1}^i$ and $\mathcal{N}_{\text{SM}}^i$ are the total signal events from U_1 and the SM background in the i th bin, respectively. The total signal events are composed of \mathcal{N}^p , \mathcal{N}^s , and \mathcal{N}^{nr} from Eqs. (A2), (A4), and (A6),

respectively. The details on how to calculate $\mathcal{N}_{U_1}^i$ for different scenarios is sketched in Appendix A. For the error $\Delta\mathcal{N}^i$, we use

$$\Delta\mathcal{N}^i = \sqrt{(\Delta\mathcal{N}_{\text{stat}}^i)^2 + (\Delta\mathcal{N}_{\text{sys}}^i)^2}, \quad (\text{B3})$$

where $\Delta\mathcal{N}_{\text{stat}}^i = \sqrt{\mathcal{N}_D^i}$ and we assume a uniform 10% systematic error, i.e., $\Delta\mathcal{N}_{\text{sys}}^i = \delta^i \times \mathcal{N}_D^i$ with $\delta^i = 0.1$.

- (2) In every scenario, for some discrete benchmark values of $M_{U_1} = M_{U_1}^b$, we compute the minimum of χ^2 as $\chi_{\text{min}}^2(M_{U_1}^b)$ by varying the couplings λ .
- (3) In one-coupling scenarios (like Scenario RD1A, Scenario RK1A, etc.), we obtain the 1σ and 2σ confidence level upper limits on the coupling at $M_{U_1} = M_{U_1}^b$ from the values of λ for which $\Delta\chi^2(M_{U_1}^b, \lambda) = \chi^2(M_{U_1}^b, \lambda) - \chi_{\text{min}}^2(M_{U_1}^b) = 1$ and 4, respectively.

In two-coupling scenarios (like Scenario RD2A, Scenario RK2A, etc.), we do the same, except we obtain the 1σ and 2σ limits (contours) from the 2-variable limits on $\Delta\chi^2$; i.e., we solve $\Delta\chi^2(M_{U_1}^b, \lambda_1, \lambda_2) = \chi^2(M_{U_1}^b, \lambda_1, \lambda_2) - \chi_{\text{min}}^2(M_{U_1}^b) = 2.30$ and 6.17, respectively.

Similarly, we can obtain the limits for the scenarios with $n(\geq 2)$ free couplings by using the n -variable ranges for $\Delta\chi^2$.

- (4) We obtain the limits for arbitrary values of M_{U_1} by interpolating the limits for the benchmark masses.

-
- [1] J. P. Lees *et al.* (BABAR Collaboration), Evidence for an Excess of $\bar{B} \rightarrow D^{(*)}\tau^-\bar{\nu}_\tau$ Decays, *Phys. Rev. Lett.* **109**, 101802 (2012).
 - [2] J. P. Lees *et al.* (BABAR Collaboration), Measurement of an excess of $\bar{B} \rightarrow D^{(*)}\tau^-\bar{\nu}_\tau$ decays and implications for charged Higgs bosons, *Phys. Rev. D* **88**, 072012 (2013).
 - [3] R. Aaij *et al.* (LHCb Collaboration), Test of Lepton Universality Using $B^+ \rightarrow K^+\ell^+\ell^-$ Decays, *Phys. Rev. Lett.* **113**, 151601 (2014).
 - [4] R. Aaij *et al.* (LHCb Collaboration), Test of lepton universality with $B^0 \rightarrow K^{*0}\ell^+\ell^-$ decays, *J. High Energy Phys.* **08** (2017) 055.
 - [5] R. Aaij *et al.* (LHCb Collaboration), Measurement of the Ratio of Branching Fractions $\mathcal{B}(\bar{B}^0 \rightarrow D^{*+}\tau^-\bar{\nu}_\tau)/\mathcal{B}(\bar{B}^0 \rightarrow D^{*+}\mu^-\bar{\nu}_\mu)$, *Phys. Rev. Lett.* **115**, 111803 (2015); Erratum, *Phys. Rev. Lett.* **115**, 159901 (2015).
 - [6] R. Aaij *et al.* (LHCb Collaboration), Measurement of the Ratio of the $B^0 \rightarrow D^{*+}\tau^+\nu_\tau$ and $B^0 \rightarrow D^{*+}\mu^+\nu_\mu$ Branching Fractions Using Three-Prong τ -Lepton Decays, *Phys. Rev. Lett.* **120**, 171802 (2018).
 - [7] R. Aaij *et al.* (LHCb Collaboration), Test of Lepton Flavor Universality by the measurement of the $B^0 \rightarrow D^{*+}\tau^+\nu_\tau$ branching fraction using three-prong τ decays, *Phys. Rev. D* **97**, 072013 (2018).
 - [8] M. Huschle *et al.* (Belle Collaboration), Measurement of the branching ratio of $\bar{B} \rightarrow D^{(*)}\tau^-\bar{\nu}_\tau$ relative to $\bar{B} \rightarrow D^{(*)}\ell^-\bar{\nu}_\ell$ decays with hadronic tagging at Belle, *Phys. Rev. D* **92**, 072014 (2015).
 - [9] Y. Sato *et al.* (Belle Collaboration), Measurement of the branching ratio of $\bar{B}^0 \rightarrow D^{*+}\tau^-\bar{\nu}_\tau$ relative to $\bar{B}^0 \rightarrow D^{*+}\ell^-\bar{\nu}_\ell$ decays with a semileptonic tagging method, *Phys. Rev. D* **94**, 072007 (2016).
 - [10] S. Hirose *et al.* (Belle Collaboration), Measurement of the τ Lepton Polarization and $R(D^*)$ in the Decay $\bar{B} \rightarrow D^{*+}\tau^-\bar{\nu}_\tau$, *Phys. Rev. Lett.* **118**, 211801 (2017).
 - [11] S. Hirose *et al.* (Belle Collaboration), Measurement of the τ lepton polarization and $R(D^*)$ in the decay $\bar{B} \rightarrow D^{*+}\tau^-\bar{\nu}_\tau$

- with one-prong hadronic τ decays at Belle, *Phys. Rev. D* **97**, 012004 (2018).
- [12] D. Bigi and P. Gambino, Revisiting $B \rightarrow D\ell\nu$, *Phys. Rev. D* **94**, 094008 (2016).
- [13] F.U. Bernlochner, Z. Ligeti, M. Papucci, and D.J. Robinson, Combined analysis of semileptonic B decays to D and D^* : $R(D^{(*)})$, $|V_{cb}|$, and new physics, *Phys. Rev. D* **95**, 115008 (2017); Erratum, *Phys. Rev. D* **97**, 059902 (2018).
- [14] D. Bigi, P. Gambino, and S. Schacht, $R(D^*)$, $|V_{cb}|$, and the heavy quark symmetry relations between form factors, *J. High Energy Phys.* **11** (2017) 061.
- [15] S. Jaiswal, S. Nandi, and S. K. Patra, Extraction of $|V_{cb}|$ from $B \rightarrow D^{(*)}\ell\nu_\ell$ and the Standard Model predictions of $R(D^{(*)})$, *J. High Energy Phys.* **12** (2017) 060.
- [16] Y. Amhis *et al.* (HFLAV Collaboration), Averages of b -hadron, c -hadron, and τ -lepton properties as of summer 2016, *Eur. Phys. J. C* **77**, 895 (2017). We have used the Spring 2019 averages from <https://hflav-eos.web.cern.ch/hflav-eos/semi/spring19/html/RDsDsstar/RDRDs.html>. For regular updates see <https://hflav.web.cern.ch/content/semileptonic-b-decays>.
- [17] R. Aaij *et al.* (LHCb Collaboration), Search for Lepton Universality Violation in $B^+ \rightarrow K^+\ell^+\ell^-$ Decays, *Phys. Rev. Lett.* **122**, 191801 (2019).
- [18] R. Aaij *et al.* (LHCb Collaboration), Test of lepton universality in beauty-quark decays, [arXiv:2103.11769](https://arxiv.org/abs/2103.11769).
- [19] G. Hiller and F. Kruger, More model-independent analysis of $b \rightarrow s$ processes, *Phys. Rev. D* **69**, 074020 (2004).
- [20] M. Bordone, G. Isidori, and A. Pattori, On the Standard Model predictions for R_K and R_{K^*} , *Eur. Phys. J. C* **76**, 440 (2016).
- [21] R. Alonso, B. Grinstein, and J. Martin Camalich, Lepton universality violation and lepton flavor conservation in B -meson decays, *J. High Energy Phys.* **10** (2015) 184.
- [22] L. Calibbi, A. Crivellin, and T. Ota, Effective Field Theory Approach to $b \rightarrow s\ell\ell^{(\prime)}$, $B \rightarrow K^{(*)}\nu\bar{\nu}$ and $B \rightarrow D^{(*)}\tau\nu$ with Third Generation Couplings, *Phys. Rev. Lett.* **115**, 181801 (2015).
- [23] S. Fajfer and N. Košnik, Vector leptoquark resolution of R_K and $R_{D^{(*)}}$ puzzles, *Phys. Lett. B* **755**, 270 (2016).
- [24] R. Barbieri, G. Isidori, A. Pattori, and F. Senia, Anomalies in B -decays and $U(2)$ flavour symmetry, *Eur. Phys. J. C* **76**, 67 (2016).
- [25] D. Bečirević, N. Košnik, O. Sumensari, and R. Zukanovich Funchal, Palatable leptoquark scenarios for lepton flavor violation in exclusive $b \rightarrow s\ell_1\ell_2$ modes, *J. High Energy Phys.* **11** (2016) 035.
- [26] S. Sahoo, R. Mohanta, and A. K. Giri, Explaining the R_K and $R_{D^{(*)}}$ anomalies with vector leptoquarks, *Phys. Rev. D* **95**, 035027 (2017).
- [27] B. Bhattacharya, A. Datta, J.-P. Guévin, D. London, and R. Watanabe, Simultaneous explanation of the R_K and $R_{D^{(*)}}$ puzzles: A model analysis, *J. High Energy Phys.* **01** (2017) 015.
- [28] M. Duraisamy, S. Sahoo, and R. Mohanta, Rare semi-leptonic $B \rightarrow K(\pi)l_i^-l_j^+$ decay in a vector leptoquark model, *Phys. Rev. D* **95**, 035022 (2017).
- [29] D. Buttazzo, A. Greljo, G. Isidori, and D. Marzocca, B-physics anomalies: A guide to combined explanations, *J. High Energy Phys.* **11** (2017) 044.
- [30] N. Assad, B. Fornal, and B. Grinstein, Baryon number and lepton universality violation in leptoquark and diquark models, *Phys. Lett. B* **777**, 324 (2018).
- [31] L. Calibbi, A. Crivellin, and T. Li, Model of vector leptoquarks in view of the B -physics anomalies, *Phys. Rev. D* **98**, 115002 (2018).
- [32] M. Blanke and A. Crivellin, B Meson Anomalies in a Pati-Salam Model within the Randall-Sundrum Background, *Phys. Rev. Lett.* **121**, 011801 (2018).
- [33] A. Greljo and B. A. Stefanek, Third family quark-lepton unification at the TeV scale, *Phys. Lett. B* **782**, 131 (2018).
- [34] S. Sahoo and R. Mohanta, Impact of vector leptoquark on $\bar{B} \rightarrow \bar{K}^*l^+l^-$ anomalies, *J. Phys. G* **45**, 085003 (2018).
- [35] J. Kumar, D. London, and R. Watanabe, Combined explanations of the $b \rightarrow s\mu^+\mu^-$ and $b \rightarrow c\tau^-\bar{\nu}$ anomalies: A general model analysis, *Phys. Rev. D* **99**, 015007 (2019).
- [36] A. Crivellin, C. Greub, D. Müller, and F. Saturnino, Importance of Loop Effects in Explaining the Accumulated Evidence for New Physics in B Decays with a Vector Leptoquark, *Phys. Rev. Lett.* **122**, 011805 (2019).
- [37] A. Angelescu, D. Bečirević, D. Faroughy, and O. Sumensari, Closing the window on single leptoquark solutions to the B -physics anomalies, *J. High Energy Phys.* **10** (2018) 183.
- [38] J. Aebischer, A. Crivellin, and C. Greub, QCD improved matching for semileptonic B decays with leptoquarks, *Phys. Rev. D* **99**, 055002 (2019).
- [39] B. Chauhan and S. Mohanty, Leptoquark solution for both the flavor and ANITA anomalies, *Phys. Rev. D* **99**, 095018 (2019).
- [40] B. Fornal, S. A. Gadam, and B. Grinstein, Left-right SU(4) vector leptoquark model for flavor anomalies, *Phys. Rev. D* **99**, 055025 (2019).
- [41] M. J. Baker, J. Fuentes-Martín, G. Isidori, and M. König, High- p_T signatures in vector-leptoquark models, *Eur. Phys. J. C* **79**, 334 (2019).
- [42] C. Hati, J. Kriewald, J. Orloff, and A. Teixeira, A nonunitary interpretation for a single vector leptoquark combined explanation to the B -decay anomalies, *J. High Energy Phys.* **12** (2019) 006.
- [43] C. Cornella, J. Fuentes-Martín, and G. Isidori, Revisiting the vector leptoquark explanation of the B-physics anomalies, *J. High Energy Phys.* **07** (2019) 168.
- [44] L. Da Rold and F. Lamagna, A vector leptoquark for the B-physics anomalies from a composite GUT, *J. High Energy Phys.* **12** (2019) 112.
- [45] K. Cheung, Z.-R. Huang, H.-D. Li, C.-D. Lü, Y.-N. Mao, and R.-Y. Tang, Revisit to the $b \rightarrow c\tau\nu$ transition: In and beyond the SM, *Nucl. Phys.* **B965**, 115354 (2021).
- [46] P. Bhupal Dev, R. Mohanta, S. Patra, and S. Sahoo, Unified explanation of flavor anomalies, radiative neutrino masses, and ANITA anomalous events in a vector leptoquark model, *Phys. Rev. D* **102**, 095012 (2020).
- [47] S. Kumbhakar and R. Mohanta, Investigating the effect of U_1 vector leptoquark on $b \rightarrow u\tau\bar{\nu}$ mediated B decays, *J. Phys. G* **48**, 075006 (2021).

- [48] S. Iguro, M. Takeuchi, and R. Watanabe, Testing leptoquark/EFT in $\bar{B} \rightarrow D^{(*)} l \bar{\nu}$ at the LHC, *Eur. Phys. J. C* **81**, 406 (2021).
- [49] C. Hati, J. Kriewald, J. Orloff, and A. Teixeira, The fate of vector leptoquarks: The impact of future flavour data, [arXiv:2012.05883](https://arxiv.org/abs/2012.05883).
- [50] J. Alda, J. Guasch, and S. Penaranda, Anomalies in B mesons decays: A phenomenological approach, [arXiv:2012.14799](https://arxiv.org/abs/2012.14799).
- [51] T. Mandal, S. Mitra, and S. Seth, Pair production of scalar leptoquarks at the LHC to NLO parton shower accuracy, *Phys. Rev. D* **93**, 035018 (2016).
- [52] D. Das, C. Hati, G. Kumar, and N. Mahajan, Towards a unified explanation of $R_{D^{(*)}}$, R_K and $(g-2)_\mu$ anomalies in a left-right model with leptoquarks, *Phys. Rev. D* **94**, 055034 (2016).
- [53] P. Bandyopadhyay and R. Mandal, Vacuum stability in an extended standard model with a leptoquark, *Phys. Rev. D* **95**, 035007 (2017).
- [54] U. K. Dey, D. Kar, M. Mitra, M. Spannowsky, and A. C. Vincent, Searching for leptoquarks at IceCube and the LHC, *Phys. Rev. D* **98**, 035014 (2018).
- [55] P. Bandyopadhyay and R. Mandal, Revisiting scalar leptoquark at the LHC, *Eur. Phys. J. C* **78**, 491 (2018).
- [56] U. Aydemir, D. Minic, C. Sun, and T. Takeuchi, B -decay anomalies and scalar leptoquarks in unified Pati-Salam models from noncommutative geometry, *J. High Energy Phys.* **09** (2018) 117.
- [57] S. Bansal, R. M. Capdevilla, A. Delgado, C. Kolda, A. Martin, and N. Raj, Hunting leptoquarks in monolepton searches, *Phys. Rev. D* **98**, 015037 (2018).
- [58] A. Biswas, D. Kumar Ghosh, N. Ghosh, A. Shaw, and A. K. Swain, Collider signature of U_1 Leptoquark and constraints from $b \rightarrow c$ observables, *J. Phys. G* **47**, 045005 (2020).
- [59] R. Mandal, Fermionic dark matter in leptoquark portal, *Eur. Phys. J. C* **78**, 726 (2018).
- [60] A. Biswas, A. Shaw, and A. K. Swain, Collider signature of V_2 Leptoquark with $b \rightarrow s$ observables, *Lett. High Energy Phys.* **2**, 126 (2019).
- [61] J. Roy, Probing leptoquark chirality via top polarization at the colliders, [arXiv:1811.12058](https://arxiv.org/abs/1811.12058).
- [62] A. Alves, O. J. P. Éboli, G. Grilli Di Cortona, and R. R. Moreira, Indirect and monojet constraints on scalar leptoquarks, *Phys. Rev. D* **99**, 095005 (2019).
- [63] U. Aydemir, T. Mandal, and S. Mitra, Addressing the $R_{D^{(*)}}$ anomalies with an S_1 leptoquark from $SO(10)$ grand unification, *Phys. Rev. D* **101**, 015011 (2020).
- [64] K. Chandak, T. Mandal, and S. Mitra, Hunting for scalar leptoquarks with boosted tops and light leptons, *Phys. Rev. D* **100**, 075019 (2019).
- [65] W.-S. Hou, T. Modak, and G.-G. Wong, Scalar leptoquark effects on $B \rightarrow \mu \bar{\nu}$ decay, *Eur. Phys. J. C* **79**, 964 (2019).
- [66] M. Bordone, O. Catà, and T. Feldmann, Effective theory approach to new physics with flavour: General framework and a leptoquark example, *J. High Energy Phys.* **01** (2020) 067.
- [67] R. Padhan, S. Mandal, M. Mitra, and N. Sinha, Signatures of \tilde{R}_2 class of leptoquarks at the upcoming ep colliders, *Phys. Rev. D* **101**, 075037 (2020).
- [68] A. Bhaskar, D. Das, B. De, and S. Mitra, Enhancing scalar productions with leptoquarks at the LHC, *Phys. Rev. D* **102**, 035002 (2020).
- [69] P. Bandyopadhyay, S. Dutta, and A. Karan, Investigating the production of leptoquarks by means of zeros of amplitude at photon electron collider, *Eur. Phys. J. C* **80**, 573 (2020).
- [70] L. Buonocore, U. Haisch, P. Nason, F. Tramontano, and G. Zanderighi, Lepton-Quark Collisions at the Large Hadron Collider, *Phys. Rev. Lett.* **125**, 231804 (2020).
- [71] M. Bordone, O. Cata, T. Feldmann, and R. Mandal, Constraining flavour patterns of scalar leptoquarks in the effective field theory, *J. High Energy Phys.* **03** (2021) 122.
- [72] A. Greljo and N. Selimovic, Lepton-quark fusion at hadron colliders, precisely, *J. High Energy Phys.* **03** (2021) 279.
- [73] U. Haisch and G. Polesello, Resonant third-generation leptoquark signatures at the large hadron collider, *J. High Energy Phys.* **05** (2021) 057.
- [74] P. Bandyopadhyay, S. Dutta, and A. Karan, Zeros of amplitude in the associated production of photon and leptoquark at $e-p$ collider, *Eur. Phys. J. C* **81**, 315 (2021).
- [75] A. Crivellin, D. Müller, and L. Schnell, Combined constraints on first generation leptoquarks, *Phys. Rev. D* **103**, 115023 (2021).
- [76] A. Greljo, G. Isidori, and D. Marzocca, On the breaking of lepton flavor universality in B decays, *J. High Energy Phys.* **07** (2015) 142.
- [77] D. A. Faroughy, A. Greljo, and J. F. Kamenik, Confronting lepton flavor universality violation in B decays with high- p_T tau lepton searches at LHC, *Phys. Lett. B* **764**, 126 (2017).
- [78] N. Raj, Anticipating nonresonant new physics in dilepton angular spectra at the LHC, *Phys. Rev. D* **95**, 015011 (2017).
- [79] I. Doršner, S. Fajfer, D. A. Faroughy, and N. Košnik, The role of the S_3 GUT leptoquark in flavor universality and collider searches, *J. High Energy Phys.* **10** (2017) 188.
- [80] D. Bečirević, I. Doršner, S. Fajfer, N. Košnik, D. A. Faroughy, and O. Sumensari, Scalar leptoquarks from grand unified theories to accommodate the B -physics anomalies, *Phys. Rev. D* **98**, 055003 (2018).
- [81] T. Mandal, S. Mitra, and S. Raz, $R_{D^{(*)}}$ motivated S_1 leptoquark scenarios: Impact of interference on the exclusion limits from LHC data, *Phys. Rev. D* **99**, 055028 (2019).
- [82] G. Aad *et al.* (ATLAS Collaboration), Search for Heavy Higgs Bosons Decaying Into Two Tau Leptons with the ATLAS Detector Using pp Collisions at $\sqrt{s} = 13$ TeV, *Phys. Rev. Lett.* **125**, 051801 (2020). HEPData link: <https://www.hepdata.net/record/ins1782650>.
- [83] A. M. Sirunyan *et al.* (CMS Collaboration), Search for resonant and nonresonant new phenomena in high-mass dilepton final states at $\sqrt{s} = 13$ TeV, HEPData link: <https://www.hepdata.net/record/ins1849964>.
- [84] A. Bhaskar, T. Mandal, and S. Mitra, Boosting vector leptoquark searches with boosted tops, *Phys. Rev. D* **101**, 115015 (2020).
- [85] A. M. Sirunyan *et al.* (CMS Collaboration), Constraints on models of scalar and vector leptoquarks decaying to a

- quark and a neutrino at $\sqrt{s} = 13$ TeV, *Phys. Rev. D* **98**, 032005 (2018).
- [86] G. Aad *et al.* (ATLAS Collaboration), Search for pairs of scalar leptoquarks decaying into quarks and electrons or muons in $\sqrt{s} = 13$ TeV pp collisions with the ATLAS detector, *J. High Energy Phys.* **10** (2020) 112.
- [87] M. Aaboud *et al.* (ATLAS Collaboration), Searches for third-generation scalar leptoquarks in $\sqrt{s} = 13$ TeV pp collisions with the ATLAS detector, *J. High Energy Phys.* **06** (2019) 144.
- [88] A. M. Sirunyan *et al.* (CMS Collaboration), Search for singly and pair-produced leptoquarks coupling to third-generation fermions in proton-proton collisions at $\sqrt{s} = 13$ TeV, *Phys. Lett. B* **819**, 136446 (2021).
- [89] W. Buchmuller, R. Ruckl, and D. Wyler, Leptoquarks in lepton-quark collisions, *Phys. Lett. B* **191**, 442 (1987); Erratum, *Phys. Lett. B* **448**, 320 (1999).
- [90] J. Blumlein, E. Boos, and A. Pukhov, Leptoquark pair production at ep colliders, *Mod. Phys. Lett. A* **09**, 3007 (1994).
- [91] J. Blumlein, E. Boos, and A. Kryukov, Leptoquark pair production in hadronic interactions, *Z. Phys. C* **76**, 137 (1997).
- [92] I. Doršner, S. Fajfer, A. Greljo, J. F. Kamenik, and N. Košnik, Physics of leptoquarks in precision experiments and at particle colliders, *Phys. Rep.* **641**, 1 (2016).
- [93] J. Alda, J. Guasch, and S. Penaranda, Some results on lepton flavour universality violation, *Eur. Phys. J. C* **79**, 588 (2019).
- [94] A. K. Alok, B. Bhattacharya, D. Kumar, J. Kumar, D. London, and S. U. Sankar, New physics in $b \rightarrow s\mu^+\mu^-$: Distinguishing models through CP -violating effects, *Phys. Rev. D* **96**, 015034 (2017).
- [95] M. Tanaka and R. Watanabe, New physics in the weak interaction of $\bar{B} \rightarrow D^{(*)}\tau\bar{\nu}$, *Phys. Rev. D* **87**, 034028 (2013).
- [96] S. Iguro, T. Kitahara, Y. Omura, R. Watanabe, and K. Yamamoto, D^* polarization vs $R_{D^{(*)}}$ anomalies in the leptoquark models, *J. High Energy Phys.* **02** (2019) 194.
- [97] K. Adamczyk (Belle and Belle-II Collaborations), Semitauonic B decays at Belle/Belle II, in *10th International Workshop on the CKM Unitarity Triangle*, 2019.
- [98] A. Akeroyd and C.-H. Chen, Constraint on the branching ratio of $B_c \rightarrow \tau\bar{\nu}$ from LEP1 and consequences for $R(D^{(*)})$ anomaly, *Phys. Rev. D* **96**, 075011 (2017).
- [99] M. Tanabashi *et al.* (Particle Data Group Collaboration), Review of Particle Physics, *Phys. Rev. D* **98**, 030001 (2018).
- [100] M. Bona (UTfit Collaboration), Latest results for the Unitarity Triangle fit from the UTfit Collaboration, *Proc. Sci., CKM2016* (2017) 096.
- [101] T. Inami and C. S. Lim, Effects of superheavy quarks and leptons in low-energy weak processes $K_L \rightarrow \mu\bar{\mu}$, $K^+ \rightarrow \pi^+\nu\bar{\nu}$ and $K^0 \leftrightarrow \bar{K}^0$, *Prog. Theor. Phys.* **65**, 297 (1981); Erratum, *Prog. Theor. Phys.* **65**, 1772 (1981).
- [102] L. Di Luzio, M. Kirk, and A. Lenz, Updated B_s -mixing constraints on new physics models for $b \rightarrow s\ell^+\ell^-$ anomalies, *Phys. Rev. D* **97**, 095035 (2018).
- [103] M. Algueró, B. Capdevila, A. Crivellin, S. Descotes-Genon, P. Masjuan, J. Matias *et al.*, Emerging patterns of New Physics with and without Lepton Flavour Universal contributions, *Eur. Phys. J. C* **79**, 714; **80**, 511(A) (2020).
- [104] J. Aebischer, W. Altmannshofer, D. Guadagnoli, M. Reboud, P. Stangl, and D. M. Straub, B -decay discrepancies after Moriond 2019, *Eur. Phys. J. C* **80**, 252 (2020).
- [105] M. Algueró, B. Capdevila, S. Descotes-Genon, J. Matias, and M. Novoa-Brunet, $b \rightarrow s\ell\ell$ global fits after Moriond 2021 results, in *55th Rencontres de Moriond on Electro-weak Interactions and Unified Theories, 2021* (2021), Vol. 4.
- [106] S. Bhattacharya, S. Nandi, and S. Kumar Patra, $b \rightarrow c\tau\nu_\tau$ Decays: A catalogue to compare, constrain, and correlate new physics effects, *Eur. Phys. J. C* **79**, 268 (2019).
- [107] C. Bobeth, M. Misiak, and J. Urban, Photonic penguins at two loops and m_t dependence of $BR[B \rightarrow X_s l^+ l^-]$, *Nucl. Phys.* **B574**, 291 (2000).
- [108] C. Bobeth, A. J. Buras, F. Kruger, and J. Urban, QCD corrections to $\bar{B} \rightarrow X_{d,s}\nu\bar{\nu}$, $\bar{B}_{d,s} \rightarrow \ell^+\ell^-$, $K \rightarrow \pi\nu\bar{\nu}$ and $K_L \rightarrow \mu^+\mu^-$ in the MSSM, *Nucl. Phys.* **B630**, 87 (2002).
- [109] W. Altmannshofer, C. Niehoff, P. Stangl, and D. M. Straub, Status of the $B \rightarrow K^*\mu^+\mu^-$ anomaly after Moriond 2017, *Eur. Phys. J. C* **77**, 377 (2017).
- [110] N. Vignaroli Seeking leptoquarks in the $t\bar{t}$ plus missing energy channel at the high-luminosity LHC, *Phys. Rev. D* **99**, 035021 (2019).
- [111] T. Mandal, S. Mitra, and S. Seth, Single productions of colored particles at the LHC: An example with scalar leptoquarks, *J. High Energy Phys.* **07** (2015) 028.
- [112] T. Mandal and S. Mitra, Probing color octet electrons at the LHC, *Phys. Rev. D* **87**, 095008 (2013).
- [113] T. Mandal, S. Mitra, and S. Seth, Probing compositeness with the CMS $eejj$ & eej data, *Phys. Lett. B* **758**, 219 (2016).
- [114] A. Alloul, N. D. Christensen, C. Degrande, C. Duhr, and B. Fuks, FeynRules2.0—A complete toolbox for tree-level phenomenology, *Comput. Phys. Commun.* **185**, 2250 (2014).
- [115] C. Degrande, C. Duhr, B. Fuks, D. Grellscheid, O. Mattelaer, and T. Reiter, UFO—The Universal FeynRules Output, *Comput. Phys. Commun.* **183**, 1201 (2012).
- [116] J. Alwall, R. Frederix, S. Frixione, V. Hirschi, F. Maltoni, O. Mattelaer *et al.*, The automated computation of tree-level and next-to-leading order differential cross sections, and their matching to parton shower simulations, *J. High Energy Phys.* **07** (2014) 079.
- [117] R. D. Ball *et al.*, Parton distributions with LHC data, *Nucl. Phys.* **B867**, 244 (2013).
- [118] T. Sjostrand, S. Mrenna, and P. Z. Skands, PYTHIA6.4 physics and manual, *J. High Energy Phys.* **05** (2006) 026.
- [119] M. L. Mangano, M. Moretti, F. Piccinini, and M. Treccani, Matching matrix elements and shower evolution for top-quark production in hadronic collisions, *J. High Energy Phys.* **01** (2007) 013.
- [120] S. Hoeche, F. Krauss, N. Lavesson, L. Lonnblad, M. Mangano, A. Schaliche *et al.*, Matching parton showers and matrix elements, in *HERA and the LHC: A Workshop on the implications of HERA for LHC physics: Proceedings Part A*, (CERN, 2005), <http://dx.doi.org/10.5170/CERN-2005-014>.

- [121] J. de Favereau, C. Delaere, P. Demin, A. Giammanco, V. Lemaître, A. Mertens *et al.* (DELPHES 3 Collaboration), DELPHES3, A modular framework for fast simulation of a generic collider experiment, *J. High Energy Phys.* **02** (2014) 057.
- [122] M. Cacciari, G.P. Salam, and G. Soyez, FastJet user manual, *Eur. Phys. J. C* **72**, 1896 (2012).
- [123] M. Cacciari, G.P. Salam, and G. Soyez, The anti- k_r jet clustering algorithm, *J. High Energy Phys.* **04** (2008) 063.